Optical Bound States in the Radiation Continuum: From Topological Charges to Light-Emission Applications

by

Bo Zhen

B.S., Mathematics and Physics, Tsinghua University (2008)

Submitted to the Department of Physics
in partial fulfillment of the requirements for the degree of

Doctor of Philosophy

at the

MASSACHUSETTS INSTITUTE OF TECHNOLOGY

September 2014

Signature redacted

Author . . . .
Department of Physics
August 28th, 2014

Signature redacted

Certified by . . . .
Marin Soljačić
Professor of Physics and MacArthur Fellow
Thesis Supervisor

Signature redacted

Accepted by . . . .
Professor Krishna Rajagopal
Associate Department Head for Education

Optical Bound States in the Radiation Continuum: From Topological Charges to Light-Emission Applications

by

Bo Zhen

Submitted to the Department of Physics
on August 28th, 2014, in partial fulfillment of the
requirements for the degree of
Doctor of Philosophy

Abstract

Bound states in the continuum (BICs) are unusal solutions of wave equations describing light or matter: they are discrete and spatially bounded, but exist at the same energy as a continuum of states which propagate to infinity. In this thesis, we will explore optical BICs from different perspectives, including physical intuitions, fundamental theories, sample fabrications, experimental setups, and real-life applications.

First, we demonstrate the existence of such exceptions realized in macroscopic two-dimensional periodic photonic crystals slab. The reason for these special modes to completely decouple from the continuum of free-space modes is through mismatching their symmetries. Further, we distinguish these special non-degenerate states with quality factors as high as 10^4 that extend over 10^8 unit cells from other existing modes in the system.

Then, we show BICs have profound implications in light-emission applications. When coupling these special states to emitters, we demonstrate greatly enhanced and strongly modulated spontaneous emission from organic molecules, due to the unique properties of BICs. Furthermore, these BICs enable lasing of organic molecules with threshold at least one order of magnitude lower than previous reported results.

Third, we demonstrate a different kind of BICs: those are not protected by symmetry incompatibility. We experimentally demonstrate that light can be perfectly confined in a patterned dielectric slab, even though outgoing waves (symmetry-compatible) are allowed in the surrounding medium. Such states exist stably in a general class of geometries where all of its radiation amplitudes vanish simultaneously due to destructive interference.

Finally, we provide a fundamental understanding about the nature of BICs that unify both types of BICs. We also explain the robustness of them through their topological nature. We show that both types of BICs are vortex centers in the polarization direction of far-field radiation. The robustness of these BICs is due to the existence of conserved and quantized topological charges, defined by the winding number of the polarization vectors. Such charges can only be generated or annihilated by making large changes in the system parameters, and then only according to strict rules, which we derive and test numerically.

Thesis Supervisor: Marin Soljačić
Title: Professor of Physics and MacArthur Fellow

Acknowledgments

First, I would like to thank my advisor, Prof. Marin Soljačić, for his encouragement, instruction, and endless help during the past years. He has made my PhD life exciting and joyful. It has been a great honor and pleasure working with Marin.

Second, I would like to thank Dr. Ofer Shapira. I learned everything from him in the lab and he has been a great mentor to me all these years.

Next, I would like to thank the professors I have met at MIT. Their instructions have deepen my understanding of physics and discussions with them have broaden my horizon. In particular, I thank Prof. John Joannopoulos for his insightful advices and inspiring discussions. I also thank Prof. Steven Johnson for his great help on many of my projects and wonderful instructions on nanophotonics and numerical methods. In addition, I thank Prof. Ray Ashoori for serving on my thesis committee and Prof. Nuh Gedik for advising on my academic progress. Also, I thank Prof. Dirk Englund, Prof. Scott Hughes, Prof. Senthil Todadri, Prof. Patrick Lee, Prof. Xiaogang Wen, and Prof. Barton Zwiebach for their wonderful lectures.

Then, I wish to express my deep thanks to all members of the JDJ group for their sincere friendship and fruitful discussions. Special thanks goes to Chia Wei Hsu, Jeongwon Lee, and Wenjun Qiu.

Finally, I dedicate this thesis to my family: my parents Yuliang Zhen and Jinrong Zhao, and my wife Peizhu Liu. This thesis would not be possible without their unconditioned love and unparalleled support.

Contents

List of Figures

Chapter 1

Overview

The realization of high quality factor cavities in photonic crystals has led in the past two decades to experimental observations of novel physical phenomena in both fundamental and applied research [3–14]. Modes supported by such cavities fall into two categories: 1) pure modes with infinite lifetimes that lie outside the light cone and 2) resonant modes with finite lifetimes that lie within the light cone and consequently can couple to radiation modes.

In 1929, von Neumann and Wigner proposed the first counterexample, in which they designed a quantum potential to trap an electron whose energy would normally allow coupling to outgoing waves. This concept is also known as bound states in the radiation continuum (BICs), or embedded eigenvalues. However, such artificially designed potential does not exist in reality: the trapping is destroyed by any generic perturbation to the potential. More recently, other counterexamples have been proposed theoretically in quantum systems [15–17], photonics [2, 18–20], acoustic and water waves [21, 22], and mathematics [23]. While no general explanation exists, some cases have been interpreted as two interfering resonances that leaves one resonance with zero width. Among these many proposals, most cannot be readily realized due to their inherent fragility. A different form of embedded eigenvalue has been realized in symmetry-protected systems, where no outgoing wave exists for modes of a particular symmetry. Even for these symmetry-protected BICs, there has been no direct demonstration of existence of such states.

In my thesis, I will explore optical BICs from a few aspects as follows: in Chapter 2, we provide am example of the first type of BICs (the ones protected by symmetry). These modes exist in macroscopic two-dimensional periodic photonic crystals slab. Their lifetimes are predicted to approach infinity as their crystal wavevector approaches zero within the light cone. In this chapter, we employ a centimeters square photonic crystal slab to demonstrate the existence of such unusal states. Further, we distinguish these special BICs with quality factors as high as 10^4 and extending over 10^8 unit cells from other modes in the system.

In Chapter 3, we show BICs have prefound implications in light-emission applications. The spectral and angular radiation pattern of the organic molecules placed close to the surface are dramatically modified compared to their free space emission due to the strongly altered spectral density of states presented by the PhC. Sharp spectral features in their fluorescence spectra are observed, with enhancement of the differential radiated power as high as 6.3×10^3 times. This property can be used for optical sensing and spectroscopy purposes. Furthermore, we show that the existing enhancement mechanisms induced by BICs also contribute to reduce the lasing threshold by an order of magnitude when compared to previously demonstrated laser cavities with the same gain medium.

In Chapter 4, we show a different type of BICs: those are not symmetry-protected. In this chapter, we predict and experimentally demonstrate that light can be perfectly confined in a patterned dielectric slab, even though outgoing waves are allowed in the surrounding medium. This happens when all raidaiton channels drop to 0 due to interference effects. These modes exist in a robust way: when certain system parameters are varied, these modes still exist but at a slightly different wavevector.

Despite all different explanations for different types of BICs; in Chapter 5, we provide a unifying theory about the basic nature of BICs that unify both types of BICs presented. We also provide a topological explanation on the robustness of BICs. We show that both types of BICs are essentially vortex centers in the polarization direction of far-field radiation. The robustness of these BICs is due to the existence of conserved and quantized topological charges, defined by the number of times the polarization vectors wind around the vortex centers. Such charges can only be generated or annihilated by making large changes in the system parameters, and then only according to strict rules, which we derive and test numerically.

In Chapter 6, I conclude and discuss potential research directions in this field of BICs.

Chapter 2

Observation and Differentiation of Symmetry-Protected BICs

2.1 Introduction

The realization of high quality factor cavities in photonic crystals has led in the past two decades to experimental observations of novel physical phenomena in both fundamental and applied research [3–14]. Modes supported by such cavities fall into two categories: 1) pure modes with infinite lifetimes that lie outside the light cone and 2) resonant modes with finite lifetimes that lie within the light cone and consequently can couple to radiation modes.

A proposed surprising exception to the latter involves special Fano resonances of a macroscopic two-dimensional periodic photonic crystals slab, whose lifetimes are predicted to approach infinity as their crystal wavevector, **k**, approaches zero within the light cone [24–26]. The only possibility for these special Fano resonances to completely decouple from the continuum of free-space modes is by mismatching their symmetries. It is the periodic nanostructure that determines the symmetry of the modes and the macroscopic large area that enables their approaching-to-infinity lifetime. In this chapter, we employ a centimeters square photonic crystal slab to demonstrate the existence of such unusal states. Further, we distinguish these special non-degenerate Fano resonances at $\mathbf{k}\approx 0$ with quality factors as high as 10^4 that extend over 10^8 unit cells.

The photonic crystal, fabricated using interference lithography, consists of a square lattice array of holes in Si_3N_4 layer with periodicity of 320 nm. Through angle-resolved spectral measurements and temporal coupled-mode theory, we determined the resonances' quality factors and the various physical mechanisms that govern their value. Using symmetry considerations, we elucidate the behavior of the different resonances at $\mathbf{k}\approx 0$. The physical origin of Fano resonances in PhC slabs lies in the coupling between the guided modes supported by the slab and external plane waves, which occurs because of the periodic modulation of the dielectric constant. Typically all these Fano resonances have long lifetimes or high quality factors (Q), but there is a special subset of them whose Q's have been proposed to approach infinity. In theory, in a perfect infinite periodic PhC slab, due to symmetry considerations, very unusual Fano 'resonances' at $\mathbf{k}=0$ have been predicted to completely decouple from the external world with infinite radiative quality factor (Q_{rad}) despite lying within the light cone [24–26]. For $\mathbf{k}$ near zero, these unique guided resonances have ultra-long (but finite) lifetime, providing an efficient means to couple light in and out of the slab. In practice due to the finite size of any experiment, the incoming and outgoing beams always include wavevectors with $\mathbf{k}>0$, and hence the resonance lifetime is finite.

Although this very unique behavior of Fano resonances in PhC slabs has been discussed theoretically [24–27], experimental verification of high-Q Fano resonances near $\mathbf{k}=0$ over a macroscopically large area has yet to be demonstrated. The key challenge in observing these resonances is that in practical structures, in addition to limits imposed by material absorption, fabrication imperfections partially break the crystal symmetry which results in coupling of these Fano resonances to radiating modes. In addition, the mode itself needs to extend over a macroscopic area in order to support high Q_{rad}, posing a significant fabrication challenge.

2.2 Sample fabrication and characterization

Realizing high quality-factor resonances in photonic nano-structures requires both the careful consideration of the bulk material properties and the sub-wavelength structure geometry. Material absorption sets the upper bound of the attainable quality factor, while the structure geometry can be optimized to minimize scattering due to surface roughness and non-uniformities of the periodic structure. A favorable candidate for achieving high quality factor resonances in the visible is a slab of Si_3N_4 deposited on top of microns thick oxide layer of a silicon wafer [28]. With refractive index of 2.02, Si_3N_4 provides sufficient index contrast with the SiO_2 below and air or fluids on top. We fabricated large area square lattice PhC with periodicity of 320 nm and unit cell consisting of a 55 nm deep, 160 nm in diameter cylindrical hole in a 250 nm thick Si_3N_4 layer (Fig. 2-1). Uniform periodic patterns were obtained on samples as large as 3 cm^2. We performed optical characterization of the PhC slab using a supercontinuum laser source at small incident angles, θ, measured from the normal to the PhC plane towards the x-axis. The reflection spectra as a function of angle, for two orthogonal pump polarizations are presented in Fig. 2-2(a)

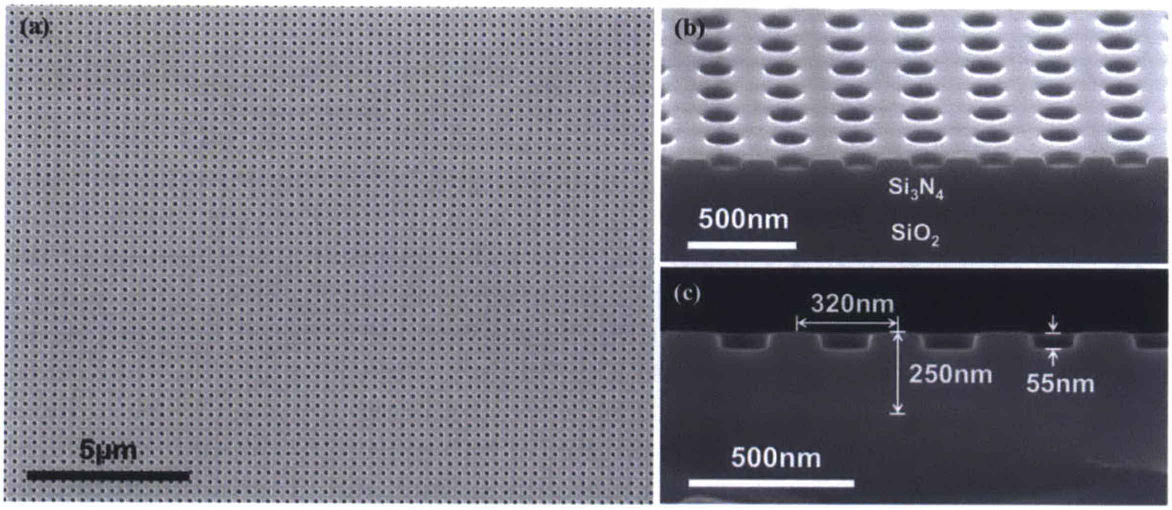

Figure 2-1: SEM images of the fabricated PhC. (a) Top-view, (b) Tilt-view, and (c) Side-view SEM images of the fabricated PhC. The structure is made of a 250 nm thick Si_3N_4 with periodic cylindrical holes on top of 6 μm thick SiO_2 layer with average period of 320 nm, average hole diameter of 160 nm, and average hole depth of 55 nm.

and 2-2(d) revealing eight energy bands.

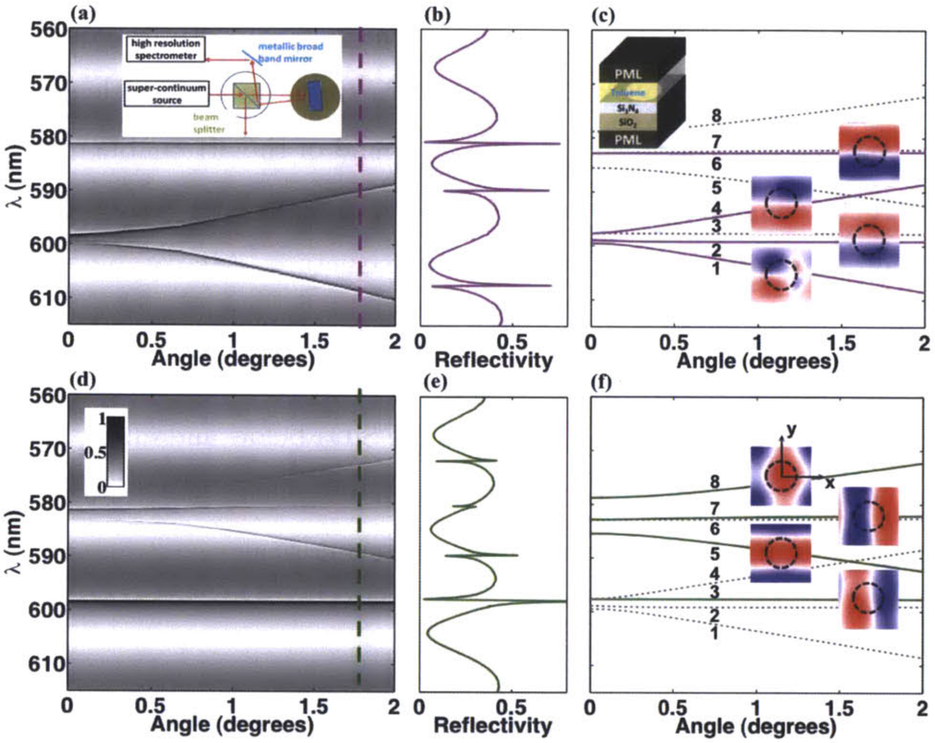

Figure 2-2: Band diagrams of the PhC obtained from reflectivity measurement and finite difference time domain (FDTD) simulation. Reflectivity measurements of the PhC with (a) E_y and (d) E_x polarized beam. The inset shows a schematic of the experimental setup. (b), (e) A slice of the reflectivity spectrum at 1.8°. (c), (f) Band diagram of the eight lowest energy modes (measured at the Γ point) of the PhC obtained from FDTD simulation. The four lower frequencies modes (numbered 1-4) are TE-like and the four higher frequencies (numbered 5-8) are TM-like. Modes excited externally by odd (even) polarized source with respect to the x-axis are colored purple (green); other modes are shown with gray dashed lines. Their E_z field profiles at the center of the Si_3N_4 layer at $\mathbf{k} = [0.01,\ 0]\cdot(2\pi/\mathrm{a})$ are also shown. Contour of the hole is shown with black dashed circle. The inset depicts a schematic of the unit computational cell used in the numerical calculation. By applying periodic boundary conditions the simulated structure becomes periodically infinite.

To corroborate these results we used finite difference time domain simulation to calculate the modes of the PhC. Fig. 2-2(c) and 2-2(f) show the dispersion curves of the eight lowest energy bands along the Γ-X line ($\mathbf{k}(\Gamma) = [0,\ 0]\cdot(2\pi/\mathrm{a})$, $\mathbf{k}(\mathrm{X}) = [0.5,\ 0]\cdot(2\pi/\mathrm{a})$, $\mathbf{k} = [k_x,\ k_y]$ and $k_x = (\omega/\mathrm{c})\sin(\theta)$). The four lower frequencies bands are TE-like (numbered 1-4) and the four higher frequencies are TM-like (numbered 5-8). The presented E_z component of all eight modes are calculated at the center of the

Si_3N_4 layer at $\mathbf{k} = [0.01, 0]\cdot(2\pi/a)$. The calculated resonant wavelengths are shifted by not more than ±0.5% from the measured spectra, well within the uncertainty of the measured periodicity or the value of the refractive index. Exception to that is the TE-like mode number 2 in Fig. 2-2(a) that appear to be very faint (almost missing): we explain the cause for this later.

It is evident from the measured spectral reflectivity of Fig. 2-2(a) and (d) that the incident beam may excite different modes of the PhC depending on its polarization. This can be understood from symmetry considerations: exciting the PhC slab with a source of one type of symmetry results in coupling to the modes of the same type of symmetry only. Note that moving away from Γ to X the symmetry group changes from C_{4v} to C_{1h} [29], reducing the number of irreducible representations from 5 to 2. Mirror reflection operation around the x-axis leaves the modes of one irreducible representation unchanged, while the modes of the other irreducible representation are altered by a factor of -1. We can determine the symmetry of each mode by examining the mode profile of its E_z component as shown in Fig. 2-2(c) and (f). Modes 1, 2, 4, and 6 are altered by a factor -1 under mirror reflection operation around the x-axis and hence excited by E_y polarized source, while modes 3, 5, 7, and 8 are unchanged under the same operation and hence excited by E_x polarized source.

Fig. 2-3 depicts the calculated $Q_{\text{rad}}^{\text{total}}$ of these eight bands. It reveals that while the doubly-degenerate (at Γ) bands 3, 4 and 6, 7 have finite $Q_{\text{rad}}^{\text{total}}$ at $\mathbf{k}\approx 0$, the singly-degenerate (at Γ) bands 1, 2, 5, and 8 have $Q_{\text{rad}}^{\text{total}}$ that go to infinity when approaching $\mathbf{k}=0$. This can be qualitatively understood from symmetry arguments. As mentioned earlier, a mode at the Γ point belongs to one of five irreducible representations of the C_{4v} point group [26,29]. One of the irreducible representations is doubly degenerate and has the same symmetry as free-space modes, while the rest are all singly degenerate and are completely decoupled from free-space modes. As a result, $Q_{\text{rad}}^{\text{total}}$ of these four singly-degenerate modes at the Γ point should be infinite despite lying within the light cone, while the doubly-degenerate modes have finite $Q_{\text{rad}}^{\text{total}}$. As we move away from Γ to X the point group becomes C_{1h} and doubly-degenerate modes split into two. The two irreducible representations of the C_{1h} point group share symmetry

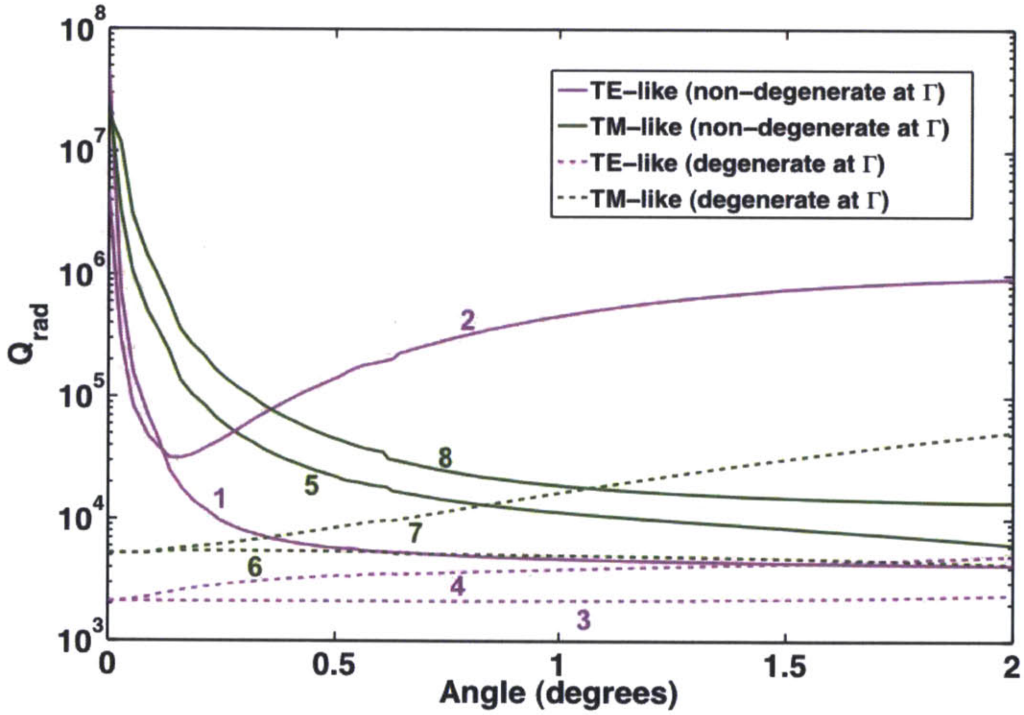

Figure 2-3: Simulation results for radiative quality factors. The high-Q singly-degenerate modes are shown with solid lines, while the doubly-degenerate (at Γ) are shown with dotted lines.

with the free-space modes and therefore $Q_{\text{rad}}^{\text{total}}$ become finite for all resonances, as is evident from the calculation.

2.3 Identification and differentiation of symmetry-protected BICs

To gain a deeper insight into the physics of the measured resonances, we developed a semi-analytical temporal coupled-mode theory mode that accounts for the presence of guided leaky resonances in the Si_3N_4 layer [3, 26]. We excited the model with an incident source propagating from the top and impinging onto the Si_3N_4 layer resonant cavity. From first-order perturbation to Maxwells equation, energy conservation considerations, and neglecting second-order effects, we attained the following expression for the reflectivity of our sample:

$$|r_{\mathrm{PhC}}|^2 = \left| r_{\mathrm{d}} - \frac{\gamma_{\mathrm{tol}} \cdot (\gamma_{\mathrm{tol}} r_{\mathrm{d}} + \gamma_{\mathrm{SiO_2}} t_{\mathrm{d}})}{i(\omega - \omega_0) + \gamma_{\mathrm{tol}}^2/2 + \gamma_{\mathrm{SiO_2}}^2/2 + 1/\tau_{\mathrm{loss}}^{\mathrm{total}}} \right|^2 \tag{2.1}$$

r_{d} and t_{d} are the complex reflection and transmission coefficients of the sample without the square lattice of cylindrical air holes. γ_{tol} and $\gamma_{\mathrm{SiO_2}}$ are the coupling strengths of the resonant mode to the top environment and the SiO$_2$ layer respectively, and can be related to the quality factors by $\gamma_{\mathrm{SiO_2}}^2 = \omega_0/Q_{\mathrm{rad}}^{\mathrm{SiO_2}}$ and $\gamma_{\mathrm{tol}}^2 = \omega_0/Q_{\mathrm{rad}}^{\mathrm{tol}}$.

From Eq. (2.1), it becomes obvious that there exist two temporal pathways: r_{d}, represents the direct transmission and reflection processes of the uniform stack, and the second term represents the guided resonances excited within the Si$_3$N$_4$ layers whose energy leaks into the far-field. It is the superposition of the two physical processes that contribute to the typical narrow Fano line shapes superimposed on a Fabry-Perot-like background that are observed in the reflectivity spectra of Fig. 2-2(b) and (e). We fitted Eq. (2.1) to the measured spectra and obtained the corresponding Q^{total}, defined as:

$$1/Q^{\mathrm{total}} = 1/Q_{\mathrm{rad}}^{\mathrm{total}} + 1/Q_{\mathrm{loss}}^{\mathrm{total}} \tag{2.2}$$

where $Q_{\mathrm{loss}}^{\mathrm{total}}$ includes losses from both material absorption and scattering due to fabrication imperfections. The results are summarized in Fig. 2-4, with an example of a fitted Fano resonance curve for the data measured at 0.8° of band 5. A complementary approach that also provides further intuitive understanding to calculate the reflection from such structure was proposed by Pottage *et al* [30].

Fig. 2-4 reveals a clear distinction between the singly-degenerate (modes 1, 2, 5, and 8) and the doubly-degenerate (modes 3, 4, 6 and 7) modes at small angles. While the measured value of Q^{total} increases when approaching **k**=0 for modes 1, 5, and 8, the doubly-degenerate modes have decreasing or fixed values. We note that although Q^{total} as high as 10^4 are observed, the calculated $Q_{\mathrm{rad}}^{\mathrm{total}}$ (Fig. 2-3) of the singly-degenerate modes are much greater at small angles, suggesting that close to **k**=0 the resonant energy decay is dominated by absorption and incoherent scattering from fabrication imperfections ($Q^{\mathrm{total}} \approx Q_{\mathrm{loss}}^{\mathrm{total}} \approx 10^4$), both of which could be

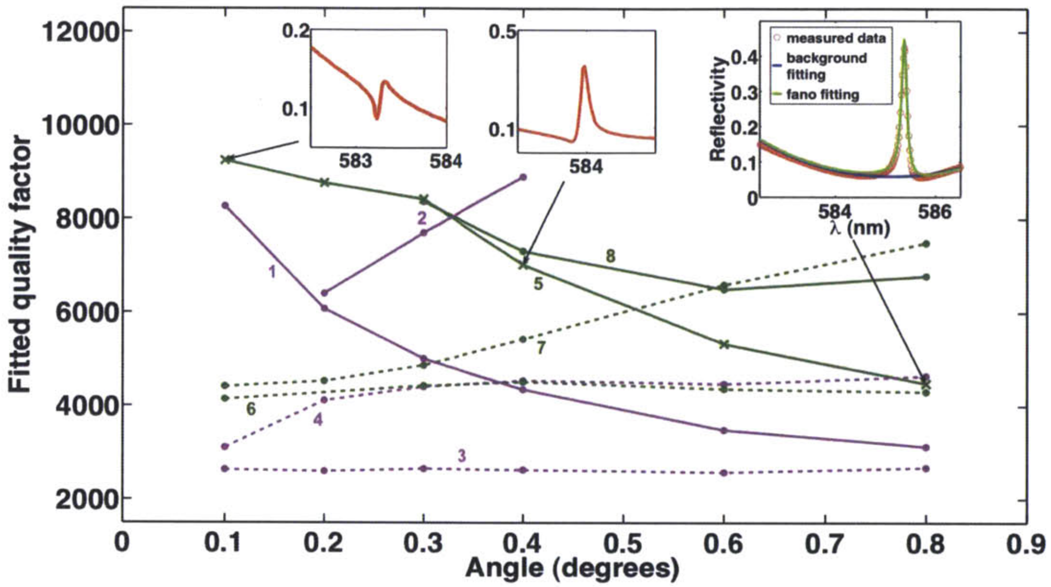

Figure 2-4: Q^{total} values retrieved by fitting Eq. (2.1) to the measured data. Insets show the reflectivity spectra of leaky mode 5 measured at three angles (0.1°, 0.4°, and 0.8°). The right inset depicts an example of the curve fitting process discussed in the text. Note the distinct higher quality factors of the singly-degenerate modes close to zero angle (i.e. zero wave vector).

significantly reduced by improving the fabrication process. On the other hand, the four low-Q bands 3, 4 and 6, 7 in Fig. 2-4 have Q^{total} values that are comparable to the calculated $Q^{\text{total}}_{\text{rad}}$ and smaller than $Q^{\text{total}}_{\text{loss}}$. Indeed, FDTD calculations of the resonant mode show that the energy confinement is approximately unchanged within the plotted range of angles, suggesting that $Q^{\text{scat}}_{\text{loss}}$ is relatively constant in the considered range of angles.

Apart from limiting the values of Q^{total} and hence the linewidth of the resonant lineshapes, the presence of relatively large scattering loss and absorption compared to far-field radiation near normal incidence leads to reduced resonant amplitudes. Conversely, the decrease of $Q^{\text{total}}_{\text{rad}}$ away from the normal provides a better match between $Q^{\text{scat}}_{\text{loss}}$ and $Q^{\text{total}}_{\text{rad}}$, which leads to an increase in the height of the features. This is consistent with Eq. (2.1), and also explains why band 2 appears only weakly in the measurement results shown in Fig. 2-2(a). Unlike other high $Q^{\text{total}}_{\text{rad}}$ modes whose values decrease rapidly away from the Γ point, the $Q^{\text{total}}_{\text{rad}}$ of the missing TE-like band

2 remains high (Fig. 2-3) for most angles, resulting in small reflectivity amplitudes which are harder to detect.

2.4 Concluding remarks

In this chapter, we experimentally differentiate and demonstrate the existence of a special class of resonances in PhCs with quality factors that could, in principle, approach infinity despite lying within the light cone. These *non-degenerate* Fano resonances are delocalized modes that decouple from the light cone states at **k**=0 due to symmetry considerations. A clear distinction between these modes and *degenerate* Fano resonances with finite Q^{total} at the Γ point is presented. With future improved fabrication that decreases the roughness and non-uniformities of the PhC slab, the current observed quality factors of $\approx 10^4$ can be significantly enhanced.

The experimental realization of this mode has four important consequences:

1 the strongly enhanced field close to the PhC surface and *the simple access* to it provides a new platform for the study of light and matter interaction;

2 it offers an easy-to-fabricate structure that supports delocalized modes with ultrahigh quality factors;

3 it can be shown from coupled mode theory [31] that up to 50% of external radiation can be coupled to these strongly confined modes in symmetric PhC slabs, when one ensures that the Q-matching condition between the radiative life-time, and the absorptive life-time is satisfied;

4 despite the macroscopically large area resonator, only a few high-Q modes are supported within a fairly broad frequency range

The delocalized nature of this mode is particularly important in applications where the interaction of an enhanced electric field with a macroscopic volume of matter can dramatically improve the performance of the process, such as in bimolecular sensing and organic light emitting devices. Furthermore, the realization of this novel resonance could enable the enhancement and the demonstration of new physical phenomena in laser physics, energy conversion, nonlinear optics, and optical filters.

Chapter 3

Enabling Enhanced Emission and Low-Threshold Lasing of Organic Molecules Using BICs

3.1 Introduction

Organic molecules are pervasive in the daily life: from natural proteins, to human synthesized fluorescing labels, to organic semiconductors. The interaction of light with such molecules is at the heart of important technological advances in biomolecular detection [32–35], fluorescent microscopy [36], and organic light emitting devices [37–40] as well as more fundamental studies of cavity quantum electrodynamics [41–43] and various types of enhanced spectroscopy [44] and sensing [45]. In all, it is frequently sought to alter [46–49] and often enhance this interaction by allowing it to occur in a typically nanostructured cavity where both the lifetime of the resonances and the optical density of states (DOS) [50] can be tailored. However, there are inherent challenges in incorporating organic molecules in such cavities: first, their dissimilar compositional structure makes it difficult to incorporate them within the high dielectric regions of the cavity where long-lifetime resonances concentrate their electromagnetic energy. Second, micro- and nanostructured cavities typically only have a small portion of their mode volumes extending outside their high-dielectric regions, making it challenging to bring external entities precisely to within that volume. Third, patterning of organic materials at the nano-scale is extremely challenging and incompatible with inorganic processes. As a result, experimental realizations of systems of excitons of organic molecules and optical resonances are limited when compared to systems of inorganic quantum nanostructures.

Here, we present and study a novel dielectric surface that enables simple incorporation of organic molecules onto a macroscopic nanostructured resonant cavity. This system demonstrates strongly enhanced interaction of light with organic molecules that are brought to within one hundred nanometers from its macroscopic surface. The surface, patterned with a sub-wavelength periodic structure, supports a special type of Fano resonances [26, 51], some of which are completely decoupled from free-space radiation due to symmetry arguments and thus maintain in principle infinitely long life time despite lying within the light cone. The uniqueness and simplicity of this system whereby delocalized resonances with ultralong life time can exist above the surface and consequently easily interact with added molecules anywhere along the surface provides a novel optofluidic platform for molecular sensing and lasing purposes. The spectral and angular radiation pattern of the organic molecules placed close to the surface are dramatically modified compared to their free space emission due to the strongly altered spectral density of states (SDOS) [50] presented by the PhC. Sharp spectral features in their fluorescence spectra are observed, with enhancement of the differential radiated power [44] as high as 6.3×10^3 times. We theoretically show that the origin of enhancement can be attributed to two mechanisms: enhancement of the local excitation field and enhancement of the extraction rate. We develop a theoretical model involving coupled mode theory (CMT) and Green's functions expansion in the basis of Bloch modes to predict the contribution of each mechanism to the total enhancement. Furthermore, we show that the two enhancement mechanisms also contribute to reduce the lasing threshold by an order of magnitude when compared to previously demonstrated laser cavities with the same gain medium (Rhodamine 6G, which was used here) [52–55]. To the best of our knowledge, this is also the first lasing demonstration of organic dye molecules using this special type of Fano resonances.

3.2 Theoretical framework of emission enhancements

We start by outlining the theoretical framework for the interaction of optical resonances and organic molecules in the weak-coupling regime. Without loss of generalities, we consider here a PhC covered with organic molecules in solution, shown schematically in Fig. 3-1. This PhC slab, made out of a periodic square array of holes, supports Fano resonances with delocalized wavefunctions and long lifetimes [26, 51]. The electronic transitions of the fluorescence process in organic molecules are shown in Fig. 3-1(a) involving the two lowest energy singlet states [44]. The interaction of light with the organic molecules can be dramatically modified in the presence of optical resonances [56–58] through two mechanisms: 1. Enhancement of the molecules' absorption by coupling the pump into a resonance mode compared to free-space coupling, Λ_{C}; 2. Enhancement of the extraction rate of generated photons into the far field in the presence of PhC compared to the free space, Λ_{T}. In this section, we derive a theoretical model for the two enhancement factors stressing effects involving the sub-wavelength structure of the resonator. Since the quantum yield of many dye molecules is close to unity [59], we assume it remains unchanged due to enhancement effects.

3.2.1 Excitation enhancement

Excitation enhancement occurs in structures that support resonances for the excitation wavelength via the enhancement of the local electric field in the site of the molecules. Since typically in nanostructured resonances the active volume of the organic material that interacts with the resonance is small (compared to the wavelength), in most cases only a small fraction of the excitation beam is absorbed. However, the local excitation field can be orders of magnitude higher than in free space when the pump is coupled to resonances with long lifetime (the pump resonant mode)

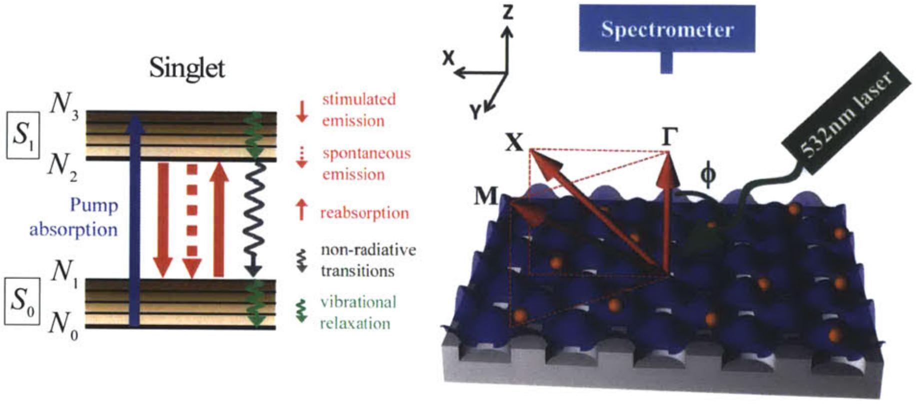

(a) **(b)**

Figure 3-1: Optofluidic platform of organic molecules coupled to Fano resonances of the macroscopic photonic crystal. (a) Schematic drawing of the two lowest singlet energy levels of a dye molecule and transitions it undergoes during fluorescence emission. (b) Schematic drawing of the experimental setup of the angle-resolved fluorescence measurements of Rhodamine 6G (R6G) dissolved in methanol at 1 mM concentration placed on top of the PhC. The grey substrate is the macroscopic PhC slab. The orange spheres are schematic drawings of the R6G molecules in solution. The blue surface represents the equal energy density surface of the Fano resonance. Fluorescence spectra of the organic solution for both cases were recorded using a high-resolution spectrometer placed close to the normal of the PhC. By tuning the position of the spectrometer, fluorescence spectra of the molecules along Γ to X and Γ to M were measured.

and therefore lead to enhanced absorption. The power absorbed by bulk molecules is given by $P^{\mathrm{B}}_{\mathrm{abs}} = (N_0 \sigma_{\mathrm{abs}} d) \times P_{\mathrm{in}}$, where σ_{abs} is the absorption cross-section of molecules, N_0 is the number density of molecules, d is the thickness of the layer that the molecules occupy and P_{in} is the pump power. Using CMT [3,31,60], the excitation enhancement can be shown to be:

$$\Lambda_{\mathrm{C}} \equiv \frac{P^{\mathrm{res}}_{\mathrm{abs}}}{P^{\mathrm{B}}_{\mathrm{abs}}} = \frac{2\lambda^{\mathrm{P}}}{\pi n d^{\mathrm{P}}_{\mathrm{eff}}} \frac{\alpha^{\mathrm{P}} (Q^{\mathrm{P}})^2}{Q^{\mathrm{P}}_{\mathrm{r}}} \tag{3.1}$$

where λ^{P} is the pump wavelength, n is the refractive index of the liquid where organic molecules are dissolved, $Q_{\mathrm{r}}^{\mathrm{P}}$ and Q^{P} are the radiative and total quality factor of the pump mode, $d_{\mathrm{eff}}^{\mathrm{P}}$ is the effective length of the evanescent tail of the pump mode into the molecule layer and α^{P} is the energy confinement of the pump mode in the molecule layer. Note that all quantities in Eq. (3.1) can be found either by FDTD simulation [29] or fitting spectral reflection measurements to CMT [51]. Excitation enhancement, Λ_{C}, is maximized when the standard Q-matching condition between the radiative and non-radiative Q of the pump mode, $Q_{\mathrm{r}}^{\mathrm{P}}$ and $Q_{\mathrm{nr}}^{\mathrm{P}}$, is satisfied [31].

To make it simpler to keep track of the various Q's that appear in the paper, we first summarize and label them with detailed explanations in Table 3.1. The processes to obtain different Q's can be summarized as follows. Firstly, we did angle-resolved reflectivity measurement of the PhC immersed in methanol. Secondly, we model the whole system from the perspective of CMT. In this CMT model, we excited the system with an incident source propagating from the top and impinging onto the $\mathrm{Si_3N_4}$ layer resonant cavity. From the first order-perturbation to the Maxwell's equation, energy conservation considerations, and by neglecting any higher order effects, we came up with a semi-analytical model that predicts the reflectivity of the PhC with the parameters of the resonances as variables, including the central frequency positions and the values of all different Q's. Finally, we fit the experimental results to the semi-analytical model and obtain all the information about the resonances, including different Q's used as the input of the current study. This whole process is identical to what has been described in the previous chapter.

3.2.2 Extraction enhancement

The second mechanism is extraction enhancement due to strong modification of the SDOS in the presence of Fano resonances. The angular emission of molecules can be dramatically altered when coupled to a macroscopic nanostructure resonance compared to in free-space. When coupled to resonances, the decay rate of a collection of randomly polarized, randomly positioned molecules into given wavevector $\mathbf{k}$ and

Table 3.1: **Summary of all the Q's.** For each resonance, total Q's represent the linewidth; non-radiative Q's are generated due to material absorption, scattering from imperfections in fabrication, and inhomogeneous broadening; radiative Q's through the top account only for the leakage towards the top surface of the PhC that participate in the pumping and fluorescing processes; while total radiative Q's account for all radiative channels and can be calculated from FDTD simulations.

	Pump mode	Fluorescence mode
total Q	Q^{P}	Q^{F}
non-radiative Q	$Q^{\mathrm{P}}_{\mathrm{nr}}$	$Q^{\mathrm{F}}_{\mathrm{nr}}$
radiative Q through the top	$Q^{\mathrm{P}}_{\mathrm{r}}$	$Q^{\mathrm{F}}_{\mathrm{r}}$
total radiative Q	$Q^{\mathrm{P,tot}}_{\mathrm{r}}$	$Q^{\mathrm{F,tot}}_{\mathrm{r}}$

frequency ω can be written as:

$$\begin{aligned}\Gamma^{\mathrm{PhC}}(\omega) &= N_0 \int_{\mathrm{gain}} \Gamma(\mathbf{r},\omega) d\mathbf{r} &(3.2)\\ &= N_0 \frac{\pi\omega|\boldsymbol{\mu}|^2}{3\hbar\epsilon_0} \sum_{\mathbf{k},\omega_{\mathbf{k}}} \int_{\mathrm{gain}} |\mathbf{E}_{\mathbf{k},\omega_{\mathbf{k}}}(\mathbf{r})|^2 d\mathbf{r} \frac{1}{\pi} \frac{\Delta\omega_{\mathbf{k}}}{(\omega-\omega_{\mathbf{k}})^2 + \Delta\omega_{\mathbf{k}}^2} &(3.3)\end{aligned}$$

Here, $\Delta\omega_{\mathbf{k}}$ is the linewidth of the resonance and $|\boldsymbol{\mu}|$ is the electric dipole momentum of the molecules. This result is achieved by decomposing the Green's function of the system with the basis of normalized Bloch modes $\mathbf{E}_{\mathbf{k},\omega_{\mathbf{k}}}(\mathbf{r})$ ($\mathbf{E}^{\mathrm{F}}(\mathbf{r})$) with finite lifetime characterized by $Q^{\mathrm{F}} = \frac{\omega_{\mathbf{k}}}{2\Delta\omega_{\mathbf{k}}}$, instead of true eigen-modes with infinitely long lifetime [61].

For a macroscopic PhC slab with area of A as discussed in this paper, we can substitute $\sum_{\mathbf{k}}$ in Eq. (3.2) with $\frac{A}{(2\pi)^2}\iint \mathrm{dk_x dk_y}$ as is commonly done in solid state physics. When evaluating Eq. (3.2) at the resonance of the PhC ($\omega = \omega_{\mathbf{k}}$), we get the differential on-resonance decay rate:

$$\begin{aligned}\Gamma^{\mathrm{PhC}}(\mathbf{k},\omega_{\mathbf{k}}) &= \frac{AN_0|\boldsymbol{\mu}|^2}{6\pi^2\hbar\epsilon_0}\alpha^{\mathrm{F}} Q^{\mathrm{F}} = \frac{N_0\pi\omega_{\mathbf{k}}|\boldsymbol{\mu}|^2}{3\hbar\epsilon_0}\alpha^{\mathrm{F}} \times \mathcal{S}(\mathbf{k},\omega_{\mathbf{k}}) &(3.4)\\ \mathcal{S}(\mathbf{k},\omega_{\mathbf{k}}) &= \frac{A}{4\pi^3\Delta\omega_{\mathbf{k}}} &(3.5)\end{aligned}$$

Here, $\alpha^{\mathrm{F}} = \int_{\mathrm{gain}} |\mathbf{E}^{\mathrm{F}}(\mathbf{r})|^2 d\mathbf{r}$ is the energy confinement of the fluorescence resonant mode in the gain medium region. $\mathcal{S}(\mathbf{k},\omega_{\mathbf{k}})$ is the spectral density of states (SDOS) of the system at $\mathbf{k}$ and $\omega_{\mathbf{k}}$. In Eq. (3.4), we clearly show the linear relation between the decay rate of molecules into crystal momentum $\mathbf{k}$ resonant frequency $\omega_{\mathbf{k}}$ and the corresponding SDOS.

Note that two assumptions were adopted in equation (3.4): 1. The gain medium is uniform and isotropic; 2. The quality factors of the resonances are large enough, such that different resonances at the same $\mathbf{k}$ are far apart from each other compared to their linewidth. Also note that the results in Eq. (3.4) is essentially related to [62]. From here on, all parameters of the fluorescence mode (Q^{F},$Q_{\mathrm{r}}^{\mathrm{F}}$,$\alpha^{\mathrm{F}}$,$\mathcal{S}$,$\Gamma^{\mathrm{PhC}}$) are for one specific mode with $(\mathbf{k}, \omega_{\mathbf{k}})$, unless specified otherwise.

Although the molecule layer is assumed to be infinitely thick on top of the PhC, only $N_{\text{eff}} = N_0 A d_{\text{eff}}^{\mathrm{F}}$ number of molecules can couple to the fluorescence resonance mode. Here $d_{\text{eff}}^{\mathrm{F}}$ is defined to be the thickness of the fluoresncece mode in the gain medium in which region $(1 - \frac{1}{e^2})$ of the total energy in the gain medium is stored. In our particular setup, $d_{\text{eff}}^{\mathrm{F}}$ was determined to be 100nm through FDTD calculations. When compared to radiation in the free space, we also need to take into account that not all but only $\frac{Q^{\mathrm{F}}}{Q_{\mathrm{r}}^{\mathrm{F}}}$ portion of generated photons can be radiated coherently to the far field when placed on top of PhC. Therefore, under the assumption that the radiation direction is close to normal, the extraction enhancement can be written as:

$$\Lambda_{\mathrm{T}}(\mathbf{k}, \omega_{\mathbf{k}}) \equiv \frac{\Gamma^{\mathrm{PhC}} \times \frac{Q^{\mathrm{F}}}{Q_{\mathrm{r}}^{\mathrm{F}}}}{\Gamma^{\text{f-s}}} = \frac{\lambda^{\mathrm{F}} \alpha^{\mathrm{F}}}{n \pi d_{\text{eff}}^{\mathrm{F}}} \frac{(Q^{\mathrm{F}})^2}{Q_{\mathrm{r}}^{\mathrm{F}}} \tag{3.6}$$

Here, λ^{F} is corresponding wavelength of the fluorescence mode. To maximize Λ_{T}, similar as in the case of Λ_{C}, one seeks to maximize α^{F} as well as to enforce the Q-matching condition of the fluorescence mode ($Q_{\mathrm{nr}}^{\mathrm{F}} = Q_{\mathrm{r}}^{\mathrm{F,tot}}$) instead of to lower $Q_{\mathrm{r}}^{\mathrm{F}}$ in general as often suggested. Similar to Eq. (3.1), all quantities in Eq. (3.6) can be obtained from FDTD calculations and spectral reflection measurements.

There are three major differences between this formalism and local optical density of states (LDOS) [50] enhancement calculations in micro-cavity systems [12,63–67]:

1. Here, we are considering the emission of a uniform and isotropic ensemble of molecules placed on a periodic macroscopic PhC into fixed crystal momentum

$\mathbf{k}$ at $\omega_{\mathbf{k}}$, which is proportional to the SDOS of the system instead of the LDOS (proportional to the emission of one dipole into all directions [68–72]);

2. To treat an infinitely large system, the basis adopted here to expand Green's functions are Bloch modes under periodic boundary condition instead of localized eigen-modes as often used in LDOS calculations;

3. The portion ($\frac{Q^{\mathrm{F}}}{Q_{\mathrm{r}}^{\mathrm{F}}}$) of generated photons to be radiated coherently to the far field and reach the detector is taken into account; therefore the maximizing condition changes from adopting lower $Q_{\mathrm{r}}^{\mathrm{F}}$ in general to Q-matching in consistence with [73].

3.2.3 Total enhancement

Given knowledge of the excitation and extraction enhancement, the total enhancement factor $\Lambda(\mathbf{k},\omega_{\mathbf{k}})$ can be shown to be:

$$\begin{aligned}\Lambda(\mathbf{k},\omega_{\mathbf{k}}) &= \left[\frac{\eta_{\mathrm{PhC}}}{\eta_0}\cdot\frac{2\lambda^{\mathrm{P}}\lambda^{\mathrm{F}}}{\pi^2 n^2 d_{\mathrm{eff}}^{\mathrm{P}} d_{\mathrm{eff}}^{\mathrm{F}}}\right]\times\left[d_{\mathrm{eff}}^{\mathrm{P}} a^2 \underbrace{\int_{\mathrm{gain}} |\mathbf{E}^{\mathrm{F}}(\mathbf{r})|^2 |\mathbf{E}^{\mathrm{P}}(\mathbf{r})|^2 d\mathbf{r}}_{\text{overlap integral}}\right]\times\left[\frac{(Q^{\mathrm{P}})^2}{Q_{\mathrm{r}}^{\mathrm{P}}}\cdot\frac{(Q^{\mathrm{F}})^2}{Q_{\mathrm{r}}^{\mathrm{F}}}\right]\\ &\approx \Lambda_{\mathrm{C}}\Lambda_{\mathrm{T}}(\mathbf{k},\omega_{\mathbf{k}}) \qquad (3.7)\end{aligned}$$

Here, $\mathbf{E}^{\mathrm{F}}(\mathbf{r})$ is the normalized mode profile for the fluorescence mode, and $\mathbf{E}^{\mathrm{P}}(\mathbf{r})$ is that for the pump mode. The approximation $\Lambda(\mathbf{k},\omega_{\mathbf{k}}) \approx \Lambda_{\mathrm{C}}\Lambda_{\mathrm{T}}(\mathbf{k},\omega_{\mathbf{k}})$ in Eq. (3.7) is valid under two assumptions: 1. The quantum yield of the molecules remains constant as mentioned; 2. More importantly, the normalized pump and fluorescence mode profiles are roughly uniformly distributed in similar region in space, therefore the overlap integral in Eq. (3.7) can be simplified to be $\alpha^{\mathrm{P}} \times \alpha^{\mathrm{F}}$. The latter approximation is commonly ignored in photonic systems; however, it can lead to further enhancement. Note that in many plasmonic systems, the origin of enhancement comes mostly from this mode overlap integral term and cannot be simplified.

Unlike plasmonic systems, the most significant contribution to the enhancement in photonic systems typically comes from the high Q's of the resonances and given by the last term of Eq. (3.7): $\frac{(Q^{\mathrm{P}})^2}{Q_{\mathrm{r}}^{\mathrm{P}}} \cdot \frac{(Q^{\mathrm{F}})^2}{Q_{\mathrm{r}}^{\mathrm{F}}}$. This term reaches its maximum of $\approx \frac{Q_{\mathrm{nr}}^{\mathrm{P}} Q_{\mathrm{nr}}^{\mathrm{F}}}{64}$ under the Q-matching condition as stated previously. Accordingly, to achieve the highest enhancement, a photonic system is desired to both present resonances with high radiative and non-radiative Q's and possess a "tuning" mechanism such that the Q-matching condition can be achieved. The photonic crystal presented here satisfies both of these two requirements. This structure was demonstrated to achieve non-radiative Q as high as 10^4 [51] only limited by fabrication imperfections, and radiative Q approaching infinity due to the decoupling from free space radiation based on symmetry arguments. Since the radiative Q of the resonances strongly depend on the wavevector $\mathbf{k}$ ($Q_{\mathrm{r}} \propto \frac{1}{k^2}$) at small $\mathbf{k}$, the Q-matching condition can always be satisfied at a certain small angle.

3.3 Experimental results of enhaced fluorescence emission and comparison to theory

We experimentally studied a system comprising solution of Rhodamine 6G (R6G) molecules in methanol suspended on top of a PhC slab supporting this special type of Fano resonances [51]. A schematic drawing of the setup is shown in Fig. 3-1(b), where the grey substrate is the PhC slab consisting of a square lattice of air cylindrical holes (same as in the previous chapter).

The PhC was placed in a liquid cell with a channel thickness of $d_{\mathrm{ch}} = 2$ μm and filled with R6G solution dissolved in methanol at the concentration of 1 mM. The liquid cell was mounted on a precision motorized rotating stage, where the incident angle of the laser ϕ can be precisely controlled along the $\Gamma - X$ direction. The fluorescence spectrum was collected using a spectrometer with resolution of 0.03 nm (HR4000, Ocean optics) aligned close to the normal direction, since we were mainly interested in the special Fano resonance with $\mathbf{k}$ near Γ. The dimension of the aperture in the spectrometer is about 5μm in X and 2mm in Y direction corresponding to acceptance angle of about 1°. By tuning the position of the spectrometer with a XYZ stage, we were able to detect fluorescence into different emission angles along $\Gamma - X$ and $\Gamma - M$ direction. The molecules are excited by a 532 nm continuous wave (CW) laser at the power level of 20 mW, well below the lasing threshold of the system.

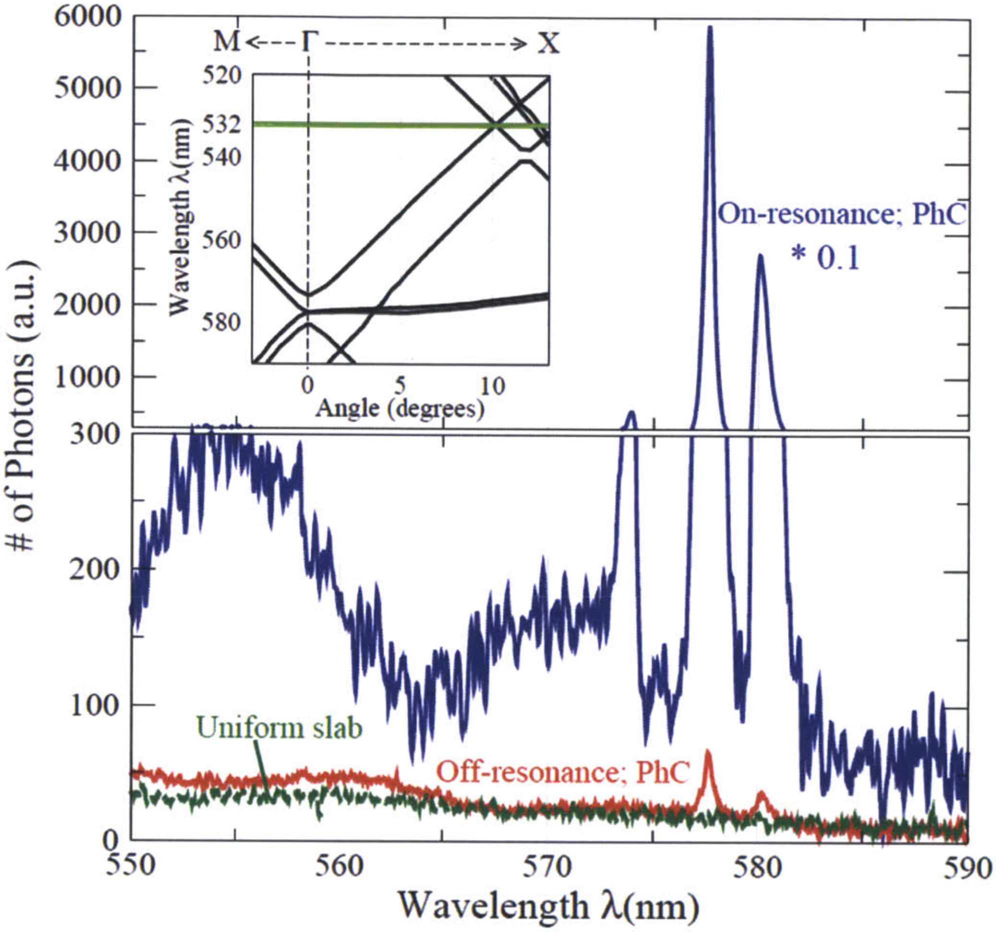

Figure 3-2: Significantly enhanced fluorescence emission from R6G molecules. Comparison of fluorescence spectra of R6G molecules measured in the normal direction, among on the PhC (solid lines) both pumped on-resonance (blue) and off-resonance (red) as well as on a uniform unpatterned slab (dashed green line). By comparing the spectra, we obtain the excitation (Λ_C^{exp}), extraction (Λ_T^{exp}), and total (Λ^{exp}) enhancement factors, which are compared with the theoretical predictions, as described in the text. The inset of the figure shows FDTD calculation results of the band structure from which the incident angle (ϕ) for on-resonance coupling is determined ($\phi_{\mathrm{on}}^{\mathrm{th}} = 10.0°$), showing good agreements with experiment ($\phi_{\mathrm{on}}^{\mathrm{exp}} = 10.02°$).

Fig. 3-2 shows comparison of the fluorescence spectra of R6G molecules measured in the normal direction for three scenarios: on an unpatterned slab (dashed green line) and on the PhC (solid lines) pumped on-resonance (blue) and off-resonance (red). The spectrometer was fixed at the normal direction of the PhC sample, while switching between on- and off- resonance coupling was achieved by tuning the incident angle of the pump, ϕ. From FDTD calculations of the band structure (inset of Fig. 3-2), on-resonance coupling angle $\phi_{\mathrm{on}}^{\mathrm{th}}$ was determined to be 10.0° agreeing well with the measured $\phi_{\mathrm{on}}^{\mathrm{exp}} = 10.02°$.

3.3.1 Comparison of excitation enhancement

In the on-resonance case the excitation field within $d_{\mathrm{eff}}^{\mathrm{P}}$ from the surface is strongly enhanced compared to off-resonance, while the remainder of the bulk layer exhibits no enhancement. The excitation enhancement can be analyzed by comparing emission spectra for on-resonance (blue) and off-resonance coupling (red). The difference between the two is solely due to excitation enhancement since the extraction enhancement Λ_{T} for the same wavelength at the same angle remains the same.

For wavelengths away from the three resonances at Γ, under off-resonance coupling, most of the emission comes from the absorption in the $d_{\mathrm{ch}} = 2\ \mu\mathrm{m}$ thick bulk layer. For on-resonance coupling, the majority (over 80%) of the absorption happens within the evanescent tail of the pump resonance mode, although $d_{\mathrm{eff}}^{\mathrm{P}} \ll d_{\mathrm{ch}}$. The absorption in $d_{\mathrm{eff}}^{\mathrm{P}}$ for on-resonance coupling can be calculated from the difference of fluorescence signal between on- and off-resonance coupling: $I_{\mathrm{on}} - I_{\mathrm{off}}$; while that for off-resonance coupling can be calculated from the thickness ratio: $I_{\mathrm{off}} \times (d_{\mathrm{eff}}^{\mathrm{P}}/d_{\mathrm{ch}})$. Here, I_{on} and I_{off} are measured fluorescence intensity for wavelengths far away from the three resonances at Γ. The effective length of the evanescent tail of the pump resonance mode in the molecule layer, $d_{\mathrm{eff}}^{\mathrm{P}}$, is defined similar to $d_{\mathrm{eff}}^{\mathrm{F}}$.

$$\Lambda_{\mathrm{exc}}^{\mathrm{exp}} = \frac{I_{\mathrm{on}} - I_{\mathrm{off}}}{I_{\mathrm{off}} \times (d_{\mathrm{eff}}^{\mathrm{P}}/d_{\mathrm{ch}})} \approx 80 \tag{3.8}$$

The theoretical prediction of excitation enhancement was calculated by plugging all quantities in Eq. (3.1). For the pump mode: $Q_{\mathrm{r}}^{\mathrm{P}} = 1.6 \times 10^4$ obtained from FDTD calculation; $Q_{\mathrm{nr}}^{\mathrm{P}} = 6300$ obtained from reflection measurements; $d_{\mathrm{eff}}^{\mathrm{P}} = 100$ nm from previous section; $\sigma_{\text{abs}} = 3.8 \times 10^{-20} m^2$ from literature [52]; $N_0 = 6 \times 10^{23} m^{-3}$; $\alpha^{\text{P}} =$ 6% from FDTD calculation; $n = 1.33$ for methanol and $\lambda^{\text{P}} = 532$ nm. Therefore, $Q^{\text{P}}_{\text{abs}} = \frac{2\pi n}{\lambda^{\text{P}} \sigma_{\text{abs}} N_0 \alpha^{\text{P}}} = 1.1 \times 10^4$. From Eq. (3.1), $\frac{P^{\text{res}}_{\text{abs}}}{P_{\text{in}}} \approx 12.7\%$, meaning the absorption in the 100 nm evanescent tail of the pump resonance is about 12.7% for on-resonance coupling. Therefore, the theoretical prediction of excitation enhancement is given by:

$$\Lambda^{\text{th}}_{\text{C}} = \frac{2\lambda^{\text{P}}}{\pi n d^{\text{P}}_{\text{eff}}} \frac{\alpha_{\text{P}} (Q^{\text{P}})^2}{Q^{\text{P}}_{\text{r}}} \approx 60 \tag{3.9}$$

showing good agreement with experimental results, $\Lambda^{\text{exp}}_{\text{C}}$. Note that the factor Q^{P}_{r} is different from the total radiative Q of the pump-mode ($Q^{\text{P,tot}}_{\text{r}}$): Q^{P}_{r} only accounts for the leakage of the resonance that can be coupled to the pump. Here, only leakage through the top surface is taken into account.

3.3.2 Comparison of extraction and total enhancements

The extraction enhancement Λ_{T} as in Eq. (3.6) depends on Q^{F}_{r}, which is strongly angular dependent near normal direction. Therefore, angle-resolved fluorescence measurements were carried out to study Λ_{T} experimentally. In total, the fluorescence signal was measured at 125 different angles up to 4.5° along $\Gamma - X$ and up to 1.5° along $\Gamma - M$ as shown in Fig. 3-3(b). Each slice on the horizontal axis represents the emission spectrum at that angle. The incident angle of the pump was fixed at 10.02° for on-resonance coupling in all measurements. For comparison, Fig. 3-3(a) shows the band structure of the PhC from FDTD calculations within the same range of angles. The bands are labeled number 1 through 5 for the simplicity of further discussion. The first feature of Fig. 3-3(b) is that the fluorescence is always maximized around the Fano resonances of the PhC . This can be intuitively understood from Eq. (3.2): the decay rate into frequency ω is proportional to $\frac{\Delta\omega_{\mathbf{k}}}{(\omega - \omega_{\mathbf{k}})^2 + (\Delta\omega_{\mathbf{k}})^2}$, which is maximized at $\omega = \omega_{\mathbf{k}}$. The second feature of Fig. 3-3(b) is the strong angular dependence similar to Λ_{T}. While similar angular dependence has been previously reported [57, 58], here we present the first rigorous quantitative model that faithfully predicts the experimental results.

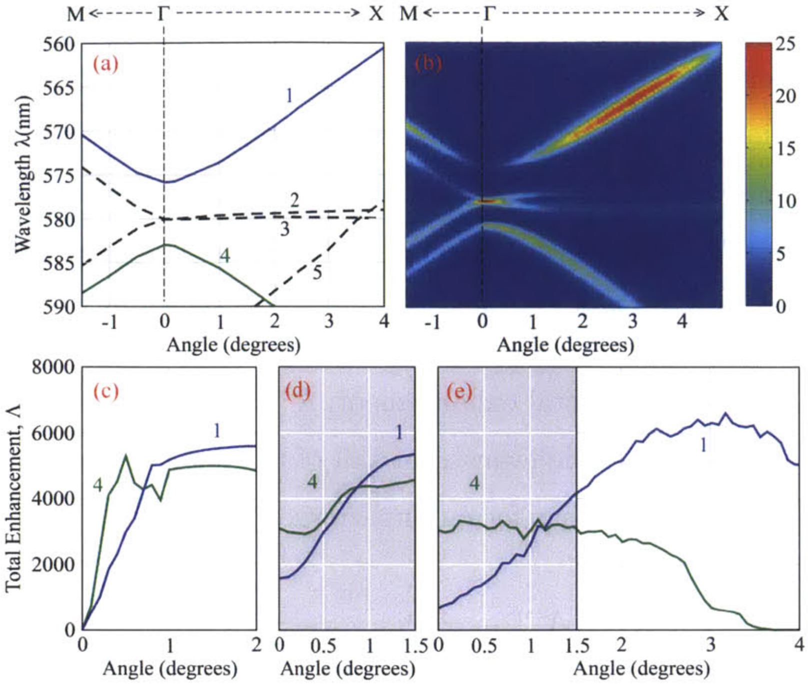

Figure 3-3: Comparison between theoretical model and experimental results of the enhancement mechanisms. (a) The band structure of the PhC along Γ to M and Γ to X directions. (b) Angle-resolved fluorescence measurements of R6G solution suspended on top of the PhC. The correspondence between the color and number of photons (arbitrary units) is given in the color bar on the side. (c) Total enhancement factors Λ^{th}, for mode 1 (blue line) and mode 4 (green line) calculated through the product of excitation enhancement $\Lambda_{\mathrm{C}}^{\mathrm{th}}$, and extraction enhancement $\Lambda_{\mathrm{T}}^{\mathrm{th}}(\mathbf{k},\omega_{\mathbf{k}})$ using the theoretical model. (d) Theoretical prediction of the averaged total enhancement factor, $\overline{\Lambda^{\mathrm{th}}}$, between 0 and 1.5°, to be compared to experiment. (e) Total enhancement factor, Λ^{exp}, extracted from experimental results in (b). Comparison between (d) and (e) for the same angle range (0 - 1.5°) shows good agreements not only in trend but also in values.

Theoretical prediction of extraction enhancement, $\Lambda_{\mathrm{T}}^{\mathrm{th}}$, for bands 1 and 4 were calculated using Eq. (3.6) within 2° along $\Gamma - X$.Here α^{F} for both mode 1 and 4 is approximately 6%. Based on this result, theoretical prediction of total enhancement Λ^{th} is plotted in Fig. 3-3(c). Note that Λ^{th} goes to zero for both bands at Γ since $Q_{\mathrm{r}}^{\mathrm{F}}$ of both modes are infinity at Γ [26, 51]. Away from Γ, $Q_{\mathrm{r}}^{\mathrm{F}}$ of both modes drops ($\propto \frac{1}{k^2}$) and $\Lambda_{\mathrm{T}}^{\mathrm{th}}$ is maximized when the Q-matching condition between $Q_{\mathrm{r}}^{\mathrm{F,tot}} \approx \frac{1}{2}Q_{\mathrm{r}}^{\mathrm{F}}$ and $Q_{\mathrm{nr}}^{\mathrm{F}}$ is reached. From [51], we see that $Q_{\mathrm{r}}^{\mathrm{F}}$ of mode 1 drops much slower than that of mode 4, which explains why Λ^{th} of mode 1 increases much slower than that of mode 4 near Γ. Finally, before we can directly compare theory to experiment, Λ^{th}

needs to be averaged over the range of $\mathbf{k}$ corresponding to the acceptance angle of the spectrometer aperture, which is narrow in the X direction (the difference of resonance frequencies of allowed $\mathbf{k}$ within corresponding acceptance angle is small compared to the resonance linewidth), but wide ($\approx 1^\circ$) in the Y direction. Due to the limitation of the angles where Q^{F} was measured in [51], averaged total enhancement $\overline{\Lambda^{\mathrm{th}}}$ can be calculated only between 0 and 1.5° along the $\Gamma - X$ as shown in Fig. 3-3(d).

Experimentally observed total enhancement, Λ^{exp}, is defined as the ratio between the fluorescence signal from the evanescent tail of the fluorescence mode $d^{\mathrm{F}}_{\mathrm{eff}}$ for on-resonance coupling case and that for on unpatterned substrate:

$$\Lambda^{\mathrm{exp}} = \frac{I^{\mathrm{on}}}{I^{\mathrm{slab}} \times (d^{\mathrm{F}}_{\mathrm{eff}}/d_{\mathrm{ch}})} \tag{3.10}$$

The maximum of total enhancement can be approximated under Q-matching between $Q^{\mathrm{F,tot}}_{\mathrm{r}}$ and $Q^{\mathrm{F}}_{\mathrm{nr}}$. Taking $Q^{\mathrm{F}}_{\mathrm{nr}} = 10^4$ [51], one can get $\Lambda^{\mathrm{th}}_{\mathrm{T}} \approx \frac{\lambda^{\mathrm{F}}}{n\pi d^{\mathrm{F}}_{\mathrm{eff}}} \frac{\alpha^{\mathrm{F}}(Q^{\mathrm{F}}_{\mathrm{nr}})^2}{8} = 104$. Combining with $\Lambda^{\mathrm{th}}_{\mathrm{C}} = 60$, the maximum value of Λ^{th} of band 1 can be approximated to be 6.24×10^3, which agrees well with the maximum value of Λ^{exp} (6.3×10^3) in Fig. 3-3(e). In Table 3.2, we also present the comparison of the enhancements for band 4 at Γ between our theoretical prediction and experimental results.

Table 3.2: **Comparison of the enhancement factors for band 4 at Γ.** For mode 4 at Γ, results of excitation enhancement Λ_{C}; extraction enhancement Λ_{T}, and total enhancement Λ from theoretical prediction through the model presented in the text are compared to the results extracted from experiments and showing good agreements with each other.

	Λ_{C}	Λ_{T}	Λ
Theoretical prediction	60	50	3×10^3
Experimental results	80	35	2.8×10^3

3.4 Effects of enhancement mechanisms on reducing lasing threshold

One direct consequence of the enhancement mechanisms is the reduction in lasing threshold of such systems. We experimentally observed significantly reduced lasing threshold of the specific organic molecules, R6G, while compared to previously reported results.

The reduction of lasing threshold in this new type of dye laser that utilize these special Fano resonances is due to two reasons. First, the excitation field is dramatically enhanced near the surface of the PhC ($\Lambda_C \gg 1$) enabling substantial absorption of the pump within a thin layer of diluted molecules near the PhC surface. The second contribution originates from the enhanced emission rate of the molecules into the lasing mode when compared to their free-space emission with similar mode volume. This enhancement can be introduced phenomenologically into the lasing rate equation [14, 74] through the spontaneous emission factor, β, which is classically defined as the ratio between the emission rate into the lasing mode and the total emission rate. The lasing threshold is typically inversely proportional to β and hence can be reduced in cases where the emission rate into the lasing mode is enhanced while the total rate remains almost constant. A rigorous CMT model of the laser dynamics of the system of organic molecules in nano-structured cavities was developed by our group elsewhere [74]. The high Q of the system also helps to reduce the lasing threshold.

The lasing experiment was carried out using the same setup as the fluorescence measurements other than replacing the CW pump with the 532 nm second harmonic of a 5 ns collimated Nd:YAG pulsed laser at 10 Hz repetition rate. Narrow emission lines were observed at $\lambda_L^4 \approx 580$ nm first and then $\lambda_L^1 \approx 575$ nm, both well within the R6G's emission spectrum. At λ_L^4, $Q^4 = 8.3 \times 10^3$ was retrieved from results in [51]. The emission spectra of the molecules when pumped below (blue) and above (red) threshold are shown in Fig. 3-4 (inset). Plugging the rates of electronic transitions in R6G and parameters of the PhC cavity into the CMT laser model [74, 75], the pulse

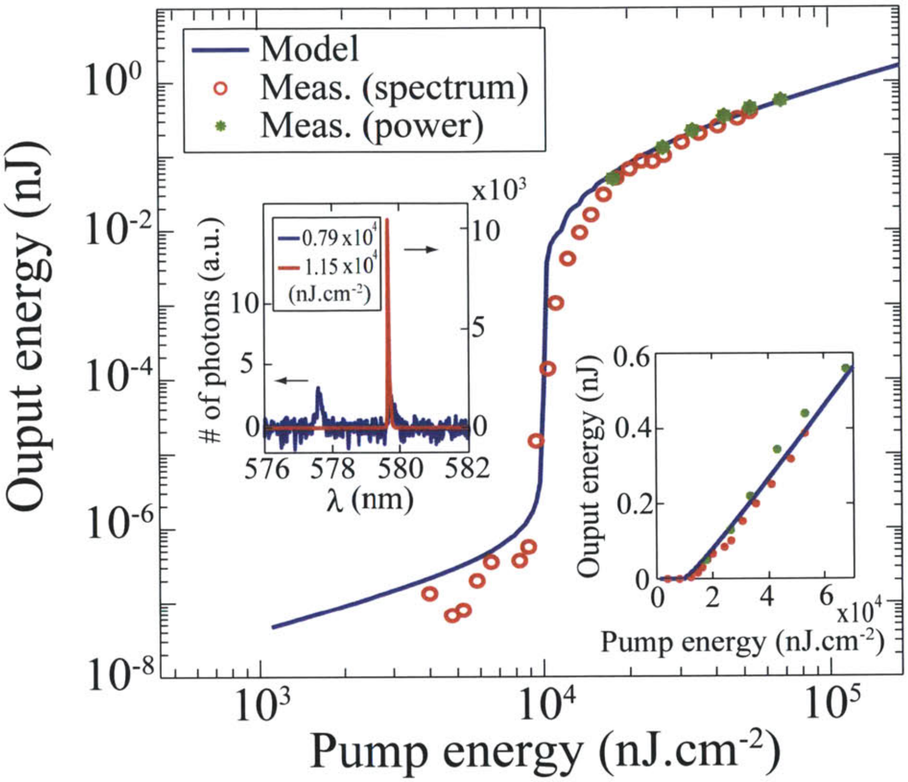

Figure 3-4: Low threshold lasing of 100 nm thin layer of R6G molecules in solution. Input-output energy characteristics of lasing through mode 4 (580 nm) under pulsed excitation. The solid lines are analytic predictions from our lasing model while red circles are energies measured using the spectrometer. Green circles are data measured with a power meter. The jump in output power clearly indicates the onset of lasing. The lower inset shows the same results in linear scale, where the output grows linearly with the pump energy beyond threshold. Top inset is the measured power spectrum of emission from the PhC slab at normal incidence below (blue) and above (red) the lasing threshold. Single-mode lasing is attained at approximately 9×10^3 nJ/cm^2(corresponding to the intensity of 1.8 kW/cm^2).

energy input-output curve is plotted against the measured data in Fig. 3-4. The jump in the log-log plot clearly indicates the onset of lasing.

The same result in linear scale is shown in the lower inset of Fig. 3-4, where the output energy grows linearly with the pump energy beyond threshold. The theoretical predictions of both threshold and slope efficiency match reasonably well with the experimental results within experimental errors. In particular, the measured threshold energy is 9×10^3 nJ/cm^2 (intensity of 1.8 kW/cm^2), an order of magnitude lower than previously demonstrated laser cavities with the gain medium [52–55]. We attribute this low lasing threshold of R6G to the two enhancement mechanisms: 1. The excitation enhancement $\Lambda_C \approx 60$ that enables 12.7% absorption of the pump energy within only 100 nm thin layer of the dye solution; 2. The rate of spontaneous emission into the lasing mode in such structure, which is proportional to $\mathcal{S}(\mathbf{k}_L, \omega_L)$, is enhanced over that in free space, yielding higher value of β.

3.5 Concluding remarks

In this chapter, we present and study a novel optofluidic platform that enables the strongly enhanced light interaction with organic molecules due to the macroscopic Fano resonances in the nano-structured cavity. We experimentally demonstrated dramatic spectral and angular redistribution of fluorescence from molecules coupled to the special Fano resonances supported by the PhC. Theoretical framework of the system was developed to explain and calculate the enhancement mechanisms showing good agreements with experiments. We found that to maximize the overall emission enhancements, Q-matching requirements need to be satisfied not only for the pump mode but also for the fluorescence mode.

Furthermore, we report lasing of 100 nm thin layer of diluted organic dye molecule solution with threshold that is an order of magnitude lower than any previously demonstrated laser systems using similar molecules. The reduction of lasing threshold was further explained by these enhancement mechanisms. This lasing experiment highlights the novelty of this system whereby organic molecules or colloidal nanoparticles can be simply introduced and interact with resonances of a macroscopic nanostructured cavity anywhere along its surface. These results present exciting opportunities in optical molecular sensing and surface light emitting devices due to the ability of simply introducing matter to the surface, the delocalized nature of the resonance modes and the enhancement mechanisms presented in the system. Finally we should point out that these results are proofs of concept only and in fact lower lasing thresholds and higher fluorescence enhancements can be achieved by optimizing the structure using the theoretical model developed here.

Chapter 4

Observation of Non-symmetry-protected BICs

4.1 Introduction

Many light confinement methods exist, but they all achieve confinement with materials or systems that forbid outgoing waves. Such systems can be implemented by metallic mirrors, by photonic band-gap materials [3], by highly disordered media (Anderson localization [76]) and, for a subset of outgoing waves, by translational symmetry (total internal reflection [3]) or rotation/reflection symmetry [51,77]. Exceptions to these examples exist only in theoretical proposals [18–20,78].

In this chapter, we predict and experimentally demonstrate that light can be perfectly confined in a patterned dielectric slab, even though outgoing waves are allowed in the surrounding medium. Technically, this is an observation of an "embedded eigenvalue" [79]—namely a bound state in a continuum of radiation modes—that is not due to symmetry incompatibility [15–23,78,80]. Such a bound state can exist stably in a general class of geometries where all of its radiation amplitudes vanish simultaneously due to destructive interference. This method to trap electromagnetic waves is also applicable to electronic [16] and mechanical waves [21,22].

The propagation of waves can be easily understood from the wave equation, but the localization of waves (creation of bound states) is more complex. Typically, wave localization can only be achieved when suitable outgoing waves either do not exist or are forbidden due to symmetry incompatibility. For electromagnetic waves, this is commonly implemented with metals, photonic bandgaps, or total internal reflections; for electron waves, this is commonly achieved with potential barriers.

In 1929, von Neumann and Wigner proposed the first counterexample [80], in which they designed a quantum potential to trap an electron whose energy would normally allow coupling to outgoing waves. However, such artificially designed potential does not exist in reality. Furthermore, the trapping is destroyed by any generic perturbation to the potential. More recently, other counterexamples have been proposed theoretically in quantum systems [15–17], photonics [18–20, 78], acoustic and water waves [21, 22], and mathematics [23]; the proposed systems in refs. 19 and 21 are most closely related to what is demonstrated here. While no general explanation exists, some cases have been interpreted as two interfering resonances that leaves one resonance with zero width [15, 16, 19]. Among these many proposals, most cannot be readily realized due to their inherent fragility. A different form of embedded eigenvalue has been realized in symmetry-protected systems [51, 77], where no outgoing wave exists for modes of a particular symmetry.

4.2 Theoretical prediction and numerical demonstration

To show that an optical bound state is feasible even when it is surrounded by symmetry-compatible radiation modes, we consider a practical structure: a dielectric slab with a square array of cylindrical holes (Fig. 4-1 (a)), an example of photonic crystal (PhC) slab [3]. The periodic geometry leads to photonic band structures, analogous to how a periodic potential in solids gives rise to electron band structures. The PhC slab supports guided resonances whose frequencies lie within the continuum of radiation modes in free space (Fig. 4-1 (b)); these resonances generally have finite lifetimes because they can couple to the free-space modes. However, using finite-

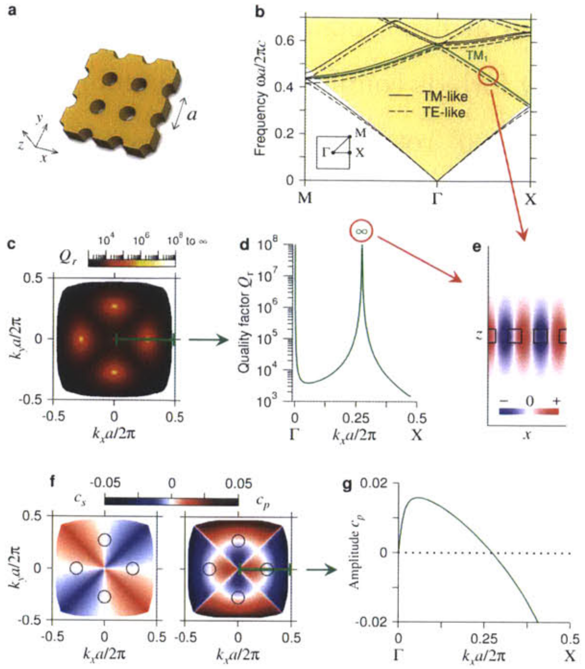

Figure 4-1: Theory predictions. a, Schematic of the photonic crystal (PhC) slab. b, Calculated band structure. Yellow shaded area indicates light cone of the surrounding medium, where there is a continuum of radiation modes in free space. The trapped state is marked with a red circle, and the TM_1 band is marked with a green line. Inset shows the first Brillouin zone. c,d, Normalized radiative lifetime Q_r of the TM_1 band calculated from FDTD, with values along the Γ-X direction shown in **d**. Below the light cone there is no radiation mode to couple to (*i.e.* total internal reflection), so Q_r is infinite. But at discrete points inside the light cone, Q_r also goes to infinity. e, Electric-field profile E_z of the trapped state, plotted on the $y = 0$ slice. f,g, Amplitudes of the s- and p-polarized outgoing planewaves for the TM_1 band, with c_p along the Γ-X direction shown in g. Black circles in f indicate k points where both c_s and c_p are zero.

difference time-domain (FDTD) simulations [81] and along with the analytical proof below, we find that the lifetime of the resonance goes to infinity at discrete k points on certain bands; here we focus on the lowest TM-like band in the continuum (referred to as TM_1 hereafter), with its lifetime shown in Fig. 4-1 (c),(d). At these seemingly unremarkable k points, light becomes perfectly confined in the slab, as is evident both from the divergent lifetime and from the field profile (Fig. 4-1 (e)). These states are no longer leaky resonances; they are eigenmodes that do not decay.

In the functional analysis literature, eigenvalues like this, which exist within the continuous spectrum of radiation modes, are called *embedded eigenvalues* [79]. Here, embedded eigenvalues occur at five k points over the first Brillouin zone. The one at Γ arises because symmetry forbids coupling to any outgoing wave [51]; the other four (which are equivalent under 90° rotations) deserve further analysis since, intuitively, they should not be confined.

To understand this unexpected disappearance of leakage, we examine the outgoing planewaves. Using Bloch's theorem [3], we let the electric and magnetic fields of the resonance be $\mathbf{E}_\mathbf{k}(\boldsymbol{\rho}, z) = e^{i\mathbf{k}\cdot\boldsymbol{\rho}}\mathbf{u}_\mathbf{k}(\boldsymbol{\rho}, z)$ and $\mathbf{H}_\mathbf{k}(\boldsymbol{\rho}, z) = e^{i\mathbf{k}\cdot\boldsymbol{\rho}}\mathbf{v}_\mathbf{k}(\boldsymbol{\rho}, z)$ where $\mathbf{k} = (k_x, k_y, 0)$, and $\mathbf{u}_\mathbf{k}$, $\mathbf{v}_\mathbf{k}$ are periodic functions in $\boldsymbol{\rho} = (x, y)$. Outside of the slab, these fields are composed of planewaves that propagate energy and evanescent waves that decay exponentially. For frequencies below the diffraction limit, the only propagating-wave amplitudes are the zeroth-order Fourier coefficients, given by

$$c_s(\mathbf{k}) = \langle \hat{\mathbf{e}}_\mathbf{k} \cdot \mathbf{u}_\mathbf{k} \rangle, \quad c_p(\mathbf{k}) = \langle \hat{\mathbf{e}}_\mathbf{k} \cdot \mathbf{v}_\mathbf{k} \rangle \tag{4.1}$$

for s and p polarizations respectively, where $\hat{\mathbf{e}}_\mathbf{k} = (k_y, -k_x, 0)/|\mathbf{k}|$ is the polarization direction of the in-plane fields, and the brackets denote spatial average on some x-y plane outside of the slab. The outgoing power from the resonance is proportional to $(|c_s|^2 + |c_p|^2)\cos\theta$, with θ being the angle of propagation. In general, c_s and c_p are two non-zero complex numbers, with a total of *four* degrees of freedom: therefore the outgoing power is unlikely to be zero when only two parameters (k_x and k_y) are varied.

However, for a certain class of geometries, the degrees of freedom can be reduced. If the structure has time-reversal symmetry $\epsilon(\mathbf{r}) = \epsilon^*(\mathbf{r})$ and inversion symmetry $\epsilon(\mathbf{r}) = \epsilon(-\mathbf{r})$, then the periodic part of the fields can be chosen to satisfy $\mathbf{u}_\mathbf{k}(\mathbf{r}) = \mathbf{u}^*_\mathbf{k}(-\mathbf{r})$ and $\mathbf{v}_\mathbf{k}(\mathbf{r}) = \mathbf{v}^*_\mathbf{k}(-\mathbf{r})$ (ref. 82). If the structure also has a mirror symmetry in z direction, then the fields must transform as ±1 under mirror flips in z (ref. 3), so the plane-parallel components must satisfy $\mathbf{u}^{\parallel}_\mathbf{k}(x, y, z) = \pm\mathbf{u}^{\parallel}_\mathbf{k}(x, y, -z)$ and $\mathbf{v}^{\parallel}_\mathbf{k}(x, y, z) = \mp\mathbf{v}^{\parallel}_\mathbf{k}(x, y, -z)$. Following these two properties, the amplitudes c_s and c_p must be purely real or purely imaginary numbers on every k point. With only *two* degrees of freedom left, it may be possible that the two amplitudes cross zero simultaneously as two parameters k_x and k_y are scanned. A simultaneous crossing at zero means no outgoing power, and therefore, a perfectly confined state. We note that such an "accidental" crossing is distinct from those where leakage is forbidden due to symmetry incompatibility between the confined mode and the radiation modes [51,77].

This disappearance of leakage may also be understood as the destructive interference between several leakage channels. The field profile inside the PhC slab can be written as a superposition of waves with different propagation constants β_z in z direction. At the slab-medium interface, each wave partially reflects back into the slab, and partially transmits into the medium to become an outgoing planewave. The transmitted waves from different β_z channels interfere, and at appropriate k points they may cancel each other. One can make this argument quantitative by writing down the corresponding equations, yet because this argument ignores the existence of evanescent waves, it is intrinsically an approximation that works best for slabs much thicker than the wavelength [21]. Nonetheless, this argument provides an intuitive physical picture that supplements the exact (yet less intuitive) mathematical proof given above.

With FDTD simulations, we confirm that both Fourier amplitudes are zero at the k points where the special trapped state is observed (Fig. 4-1 (f), (g)). The zeros of c_s on the two axes and the zeros of c_p on the diagonal lines arise from symmetry mismatch, but the zeros of c_p along the roughly circular contour are "accidental" crossings that would not be meaningful if c_p had both real and imaginary parts. We have checked that a frequency-domain eigenmode solver [82] also predicts planewave amplitudes that cross zero at these k points.

4.3 Sample fabrication and experimental setup

To experimentally confirm the existence of this trapped state, we use interference lithography to fabricate a macroscopic Si_3N_4 PhC slab ($n = 2.02$, thickness 180 nm) with a square array of cylindrical holes (periodicity 336 nm, hole diameter 160 nm), separated from the lossy silicon substrate with 6 μm of silica (Fig. 4-2 (a)). Scanning

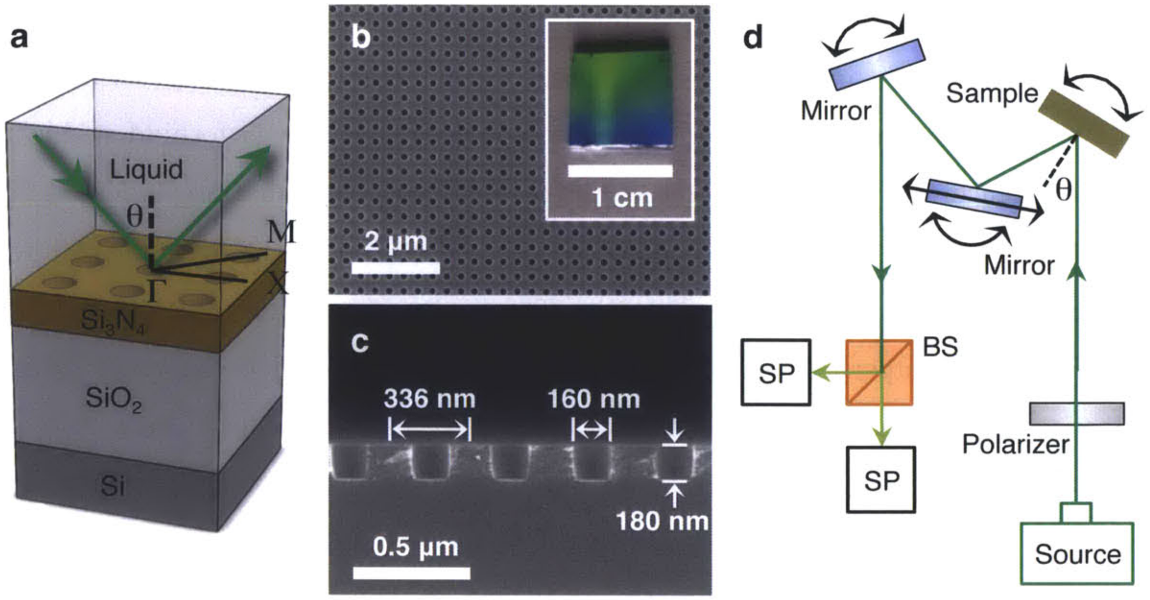

Figure 4-2: Fabricated PhC slab and the measurement setup. a, Schematic layout of the fabricated structure. The device is immersed in a liquid, index-matched to silica at 740 nm wavelength. b,c, SEM images of the structure in top view and side view. Inset of **b** shows an image of the whole PhC. d, Schematic of the setup for reflectivity measurements. BS, beamsplitter; SP, spectrometer.

electron microscope (SEM) images of the sample are shown in (Fig. 4-2 (b),(c)). The material Si_3N_4 provides low absorption and enough index contrast with the silica layer ($n = 1.46$).

The Si_3N_4 layer was grown by LPCVD on top of 6 μm thermally grown SiO_2 on a silicon wafer (LioniX), and subsequently coated with antireflection coating, a SiO_2 intermediate layer, and negative photoresist. The periodic PhC pattern was created with Mach-Zehnder interference lithography using a 325 nm He/Cd laser. Two orthogonal exposures defined the two-dimensional pattern. The interference angle was chosen for periodicity 336 nm, and the exposure time chosen for hole diameter 160 nm. After exposures, the sample was developed, and the pattern was transferred from photoresist to Si_3N_4 by reactive-ion etching; CHF_3/O_2 gas was used to etch SiO_2 and Si_3N_4, and He/O_2 gas was used to etch the antireflection coating.

To create an optically symmetric environment needed to reduce the degrees of freedom in the outgoing-wave amplitudes, we etch the holes through the entire Si_3N_4 layer, and immerse the sample in an optical liquid that is index-matched to silica. We perform angle-resolved reflectivity measurements (schematic setup shown in Fig. 4-2 (d)) to characterize the PhC sample. The source was a supercontinuum laser (SuperK Compact, NKT Photonics) with divergence angle 6×10^{-4} radian and beam-spot width 2 mm on the PhC sample at normal incidence. A polarizer selected p-polarized light, which coupled with the TM_1 band. To create σ_z symmetry, the sample was immersed in a colorless liquid with index $n = 1.454$ at 740 nm (Cargille Labs). The sample was mounted on two perpendicular motorized rotation stages: one oriented the PhC to the Γ-X direction, while the other scanned the incident angle θ. The reflected beam was split into two and collected by two spectrometers, each with a resolution of 0.05 nm (HR4000, Ocean optics). Measurements were made every 0.5° from normal incidence to 60°.

4.4 Experimental results and CMT analysis

In this section, we present the experimental results we got using the setup described in the previous section. Furthermore, we apply CMT to the reflection measurement results and extract different quality factors from the experimental results. Through this process, we demonstrate the existence of these non-symmetry-protected BICs and characterize the total quality factors we achieved.

4.4.1 Experimental results

Light incident on the PhC slab excites the guided resonances, creating sharp Fano features in the reflectivity spectrum [26]. In comparison, a perfect bound state has no Fano feature, because it is decoupled from far-field radiation. In the measured reflectivity spectrum (Fig. 4-3 (a)), we indeed observe that the Fano feature of the TM_1 band disappears near 35°. The measurements agree well with the theory prediction, shown in Fig. 4-3 (b), with the resonance wavelengths between the two differing by less than 2 nm. The measured Fano features are slightly broader than predicted, due to inhomogeneous broadening (since the measured data are averaged over many unit cells) and scattering loss introduced by disorders.

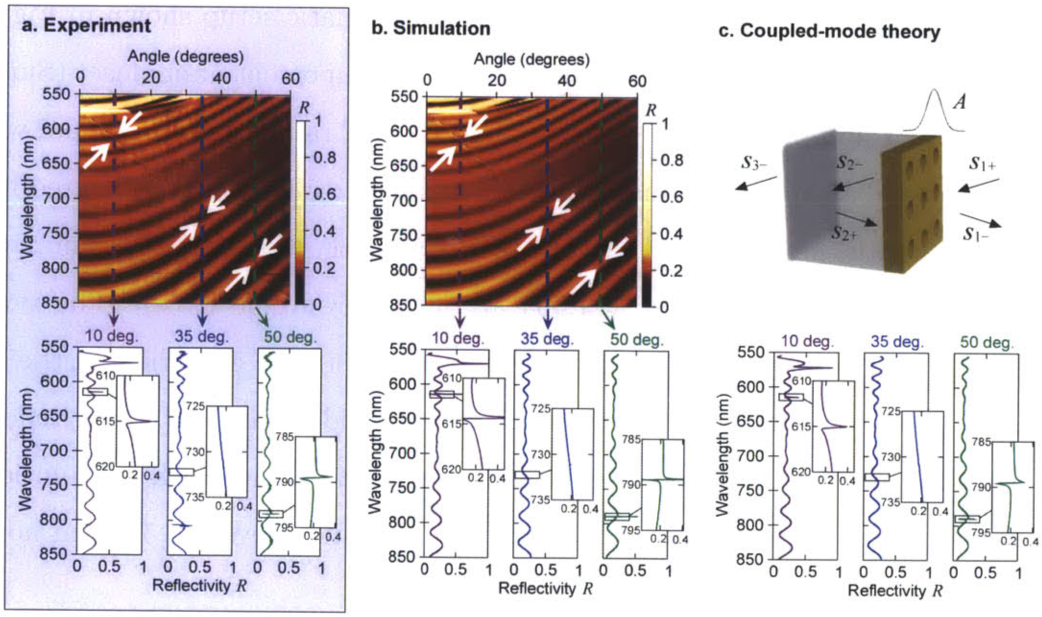

Figure 4-3: Detection of resonances from reflectivity data. a, Experimentally measured specular reflectivity for p-polarized light along Γ-X. The crucial feature of interest is the resonance, which shows up as a thin faint line (emphasized by white arrows) extending from the top-left corner of the top panel to the bottom-right corner. Disappearance of the resonance feature near 35° indicates a trapped state with no leakage. Bottom panel shows slices at three representative angles, with close-ups near the resonance features. b, Calculated p-polarized specular reflectivity using the rigorous coupled-wave analysis (RCWA) method [1] with known refractive indices and measured layer thickness. c, Top: schematic for the scattering process in temporal coupled-mode theory (CMT), which treats the resonance A and the incoming/outgoing planewaves $s_{m\pm}$ as separate entities weakly coupled to each other. Bottom: reflectivity given by the analytical CMT expression; the resonance frequency and lifetimes, which are the only unknowns in the CMT expression, are fitted from the experimental data in a.

4.4.2 CMT model and fitting

In this section, we extract the resonance lifetimes from the Fano features. In temporal coupled-mode theory (CMT), the field A of the resonance and fields $s_{m\pm}$ of the incoming/outgoing planewaves are considered separate entities that are weakly coupled to each other through their spatial overlaps[1,21]. A schematic illustration is given in Fig. 4-3 (c). The resonance decays with a radiative-decay lifetime $\tau_{\rm r}$ from leakage into the outgoing planewaves, and a non-radiative-decay lifetime $\tau_{\rm nr}$ from material absorption and disorder scattering. As we will see, the effect of $\tau_{\rm nr}$ is to broaden the resonance feature in the reflectivity spectrum; therefore it also heuristically accounts for the inhomogeneous broadening in the measured reflectivity data. Incoming planewaves excite the resonance with coupling coefficients denoted by κ_1 and κ_2. Thus we have

$$\frac{dA}{dt} = \left(-i\omega_0 - \frac{1}{\tau_{\mathrm{r}}} - \frac{1}{\tau_{\mathrm{nr}}}\right) A + \kappa_1 s_{1+} + \kappa_2 s_{2+}. \tag{4.2}$$

The planewaves on the two sides of the slab couple to each other through a direct scattering process, with transmission and reflection coefficients t_{slab} and r_{slab}. The resonance decays into the outgoing planewaves, with coupling coefficients denoted by d_1 and d_2. Therefore,

$$s_{1-} = r_{\mathrm{slab}} s_{1+} + t_{\mathrm{slab}} s_{2+} + d_1 A, \tag{4.3}$$

$$s_{2-} = t_{\mathrm{slab}} s_{1+} + r_{\mathrm{slab}} s_{2+} + d_2 A. \tag{4.4}$$

Lastly, the reflection at the silica-silicon interface (with coefficient r_{23}) and the propagation inside the silica layer impose that

$$s_{2+} = e^{2i\beta h_2} r_{23} s_{2-} \tag{4.5}$$

where $\beta = \sqrt{n_{\mathrm{SiO_2}}^2 \omega^2 / c^2 - |\mathbf{k}|^2}$ is the propagation constant in the silica layer, and h_2 is the layer's thickness. The normalization of the field amplitudes is chosen such that $|A|^2$ is the energy stored in the resonance, and $|s_{m\pm}|^2$ is the power carried by the incoming or outgoing planewaves.

Now, assume $e^{-i\omega t}$ time dependence for the resonance amplitude A. Solving equations (1–4) as a system of linear equations, we obtain

$$\frac{s_{1-}}{s_{1+}} = r_{\mathrm{slab}} + \frac{d_1 \kappa_1}{i(\omega_0 - \omega) + \tau_{\mathrm{r}}^{-1} + \tau_{\mathrm{nr}}^{-1}} + \frac{\left[t_{\mathrm{slab}} + \frac{d_1 \kappa_2}{i(\omega_0 - \omega) + \tau_{\mathrm{r}}^{-1} + \tau_{\mathrm{nr}}^{-1}}\right] \left[t_{\mathrm{slab}} + \frac{d_2 \kappa_1}{i(\omega_0 - \omega) + \tau_{\mathrm{r}}^{-1} + \tau_{\mathrm{nr}}^{-1}}\right]}{e^{-2i\beta h_2} r_{23}^{-1} - r_{\mathrm{slab}} - \frac{d_2 \kappa_2}{i(\omega_0 - \omega) + \tau_{\mathrm{r}}^{-1} + \tau_{\mathrm{nr}}^{-1}}} \tag{4.6}$$

which gives us the overall reflectivity. This expression can be simplified, as follows. First, σ_z mirror-flip symmetry of the PhC slab requires fields of the resonance to be either even or odd in z, and so $d_2 = \pm d_1$. Secondly, energy conservation requires that in the absence of input power ($s_{1+} = s_{2+} = 0$), the energy dissipated through radiative decay must be carried away by s_{1-} and s_{2-}; this leads to $|d_1|^2 = 1/\tau_r$. Thirdly, inversion symmetry I and σ_z mirror symmetry yields $I\sigma_z = C_2$ rotational symmetry about the plane normal, and a combination of time reversal symmetry and C_2 symmetry leads to $r_{\text{slab}} d_1^* + t_{\text{slab}} d_2^* + d_1 = 0$ (refs. 8, 22). A combination of these facts yields

$$d_1^2 = -\frac{1}{\tau_r}(r_{\text{slab}} \pm t_{\text{slab}}). \tag{4.7}$$

Lastly, the coupling coefficients for the incoming and for the outgoing waves are actually the same under energy conservation and time reversal requirements[1,21,22], *i.e.* $d_1 = \kappa_1$ and $d_2 = \kappa_2$. With these known properties, we can write the overall reflectivity as

$$R = \left|\frac{s_{1-}}{s_{1+}}\right|^2 = \left|r_{\text{slab}} - f(\omega) + \frac{[t_{\text{slab}} \mp f(\omega)]^2}{e^{-2i\beta h_2} r_{23}^{-1} - r_{\text{slab}} + f(\omega)}\right|^2 \tag{4.8}$$

with

$$f(\omega) = \frac{Q_r^{-1}}{2i(1-\omega/\omega_0) + Q_r^{-1} + Q_{nr}^{-1}}\left(r_{\text{slab}} \pm t_{\text{slab}}\right), \tag{4.9}$$

where $Q_r = \omega_0\tau_r/2$ and $Q_{nr} = \omega_0\tau_{nr}/2$ are the normalized lifetimes. We fit the experimentally measured reflectivity spectrum with this expression to extract the lifetime of the resonances.

We note that, the only unknowns in this reflectivity expression are the resonance frequency and the lifetimes: r_{23} is given by the Fresnel equations, and r_{slab}, t_{slab} can be approximated as the reflection and transmission coefficients of a homogeneous slab whose permittivity is equal to the spatial average of the PhC slab[19,22].

In the absence of $f(\omega)$, Eq. 4.9 reduces to the expression for multi-layer thin-film reflectivity. Therefore the Fano features are completely captured by $f(\omega)$. From equation (8), we see that the width of the Fano feature is proportional to $Q_r^{-1} + Q_{nr}^{-1}$, while the height of the feature grows with Q_r^{-1}. This confirms our intuitive understanding that, when the resonance becomes a bound state ($Q_r = \infty$), it decouples from the far field, and the Fano feature disappears.

It is straightforward to generalize this CMT expression to include multiple resonances in the spectrum; same derivation shows that we can simply replace $f(\omega)$ in Eq. 4.9 with a summation $\sum_j f^{(j)}(\omega)$ for different resonances labeled by j. Each resonance has its resonant frequency and lifetimes that are to be determined from the fitting. Lastly, we note that the $\pm$ signs relate to how the resonance fields transform under mirror flips in z. When the electric field is used to determine the phase of A and $s_{m\pm}$, we should read the upper signs for TE-like modes, lower signs for TM-like modes.

4.4.3 Fitted quality factors

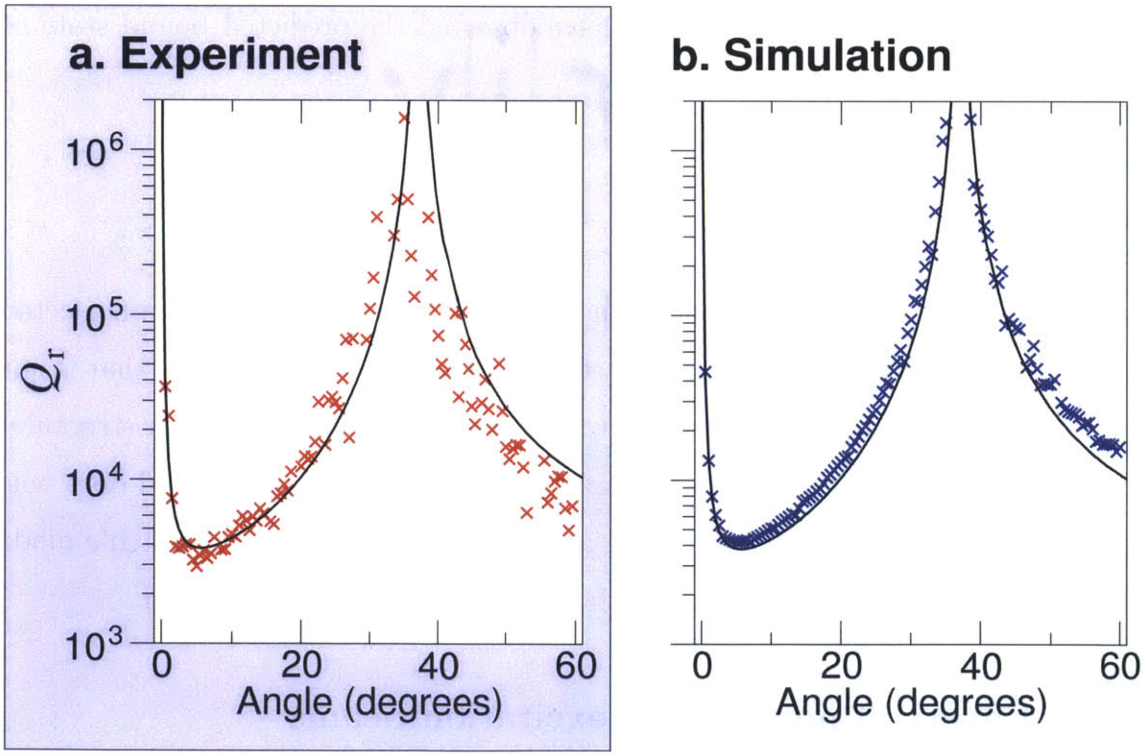

Figure 4-4: Quantitative evidence on the disappearance of leakage. a,b, Normalized radiative lifetime Q_r extracted from the experimentally-measured reflectivity spectrum (a) and the RCWA-calculated reflectivity spectrum (b). Black solid line shows prediction from FDTD.

The only unknowns in the CMT reflectivity expression are the resonance frequency and the lifetimes, which we obtain by fitting to the measured reflectivity spectrum. The fitted curves are shown in the bottom panel of Fig. 4-3 (c), and the obtained radiative Q_{r} is shown in Fig. 4-4 (a). At around 35°, Q_{r} reaches 1,000,000, near the instrument limit imposed by the resolution and signal-to-noise ratio, and in a good agreement with the values calculated from FDTD. We note that, the finite width and non-zero divergence of the excitation beam give rise to a spread of k points, leading to an upper bound of 10^{10} for the measured radiative Q_{r}; in this experiment, this is not the limiting factor for the measured Q_{r}. In comparison, the non-radiative Q_{nr} is limited to about 10^4 which is due to loss from material absorption, disorder scattering, in-plane lateral leakage, and inhomogeneous broadening. Lastly, for validation, we repeated the same fitting procedure for the simulated reflectivity spectrum, and confirmed that consistent theoretical estimates of Q_{r} are obtained (Fig. 4-4 (b)). These evidences quantitatively verify that we have observed the predicted bound state of light.

4.5 Discussion

In this section, we provide discussions on two important aspects that was neglected in previous analysis. First, what are the effects of having excitation beam that is not perfectly plane waves and what is the corresponding limitation on Q_{r} of our structure. Second, what kind of structural perturbations breaks BICs and what kind does not. Also, if there are extra benefits of having a tuning parameter that can switch a mode between a true BIC and a resonance with high Q in a controllable fashion.

4.5.1 Effects of non-perfect excitation beams

Our analysis so far assumes excitation with a perfect planewave. However, some care must be taken with the Gaussian beam from the supercontinuum source. First, the beam spot has a diameter of 2 mm at normal incidence, so the excited mode has a finite lateral size of $L \approx 2$ mm. This finite-sized mode consists of a spread of k points, with $\delta k_{\mathrm{mode}} \approx 2\pi/L \approx (2 \times 10^{-4})(2\pi/a)$. Second, the beam has a divergence angle of $\delta\theta \approx 6 \times 10^{-4}$ radian, so the source also has a spread of k points, with $\delta k_{\text{source}} \approx (2\pi/\lambda)\delta\theta \approx (3 \times 10^{-4})(2\pi/a)$. The measured radiative loss will be the averaged value within this spread of k points.

The outgoing-wave amplitude goes through zero linearly (see Fig. 1g of the main text), so the outgoing power goes as $(\Delta k)^2$ near the embedded bound states, where $\Delta k = |\mathbf{k} - \mathbf{k}_0|$ is distance from the special k point, $\mathbf{k}_0$. Specifically, FDTD simulations show that near the special trapped state studied in this paper, $Q_{\text{r}} \approx 100/(\Delta ka/2\pi)^2$. In a circular area with diameter δk, the effective Q_{r} will be $800/(\delta ka/2\pi)^2$, which is around 10^{10} for the k-point spread due to the beam. This sets the upper limit on the Q_{r} we can obtain with our source.

4.5.2 Structural perturbation that break BICs

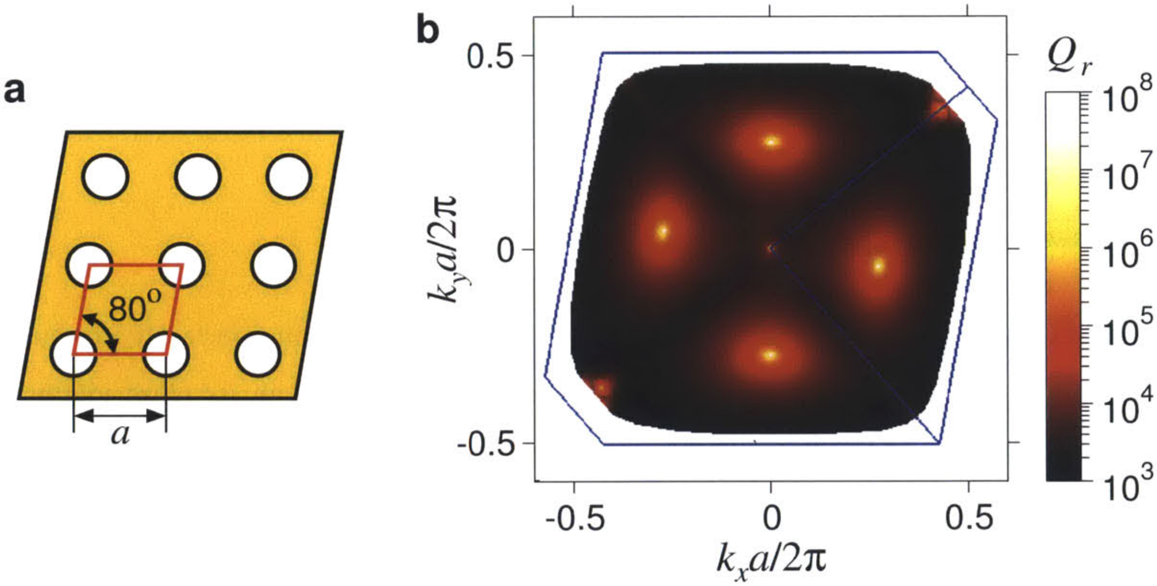

Figure 4-5: Quantitative evidence on the disappearance of leakage. a,b, Normalized radiative lifetime Q_{r} extracted from the experimentally-measured reflectivity spectrum (a) and the RCWA-calculated reflectivity spectrum (b). Black solid line shows prediction from FDTD.

The trapped state is *robust*, because small variations of the system parameters (such as cylinder diameter) only move the crossing to a different value of k_x. This robustness is crucial for our experimental realization of such states. In fact, the trapped state persists even when the C_4 rotational symmetry of the structure is broken (Fig. 4-5).

However, perturbations that break inversion or mirror symmetry will introduce additional degrees of freedom in the Fourier amplitudes, thus reducing the infinite-lifetime bound state into a long-lived leaky resonance (Fig. 4-6) unless additional tuning parameters are used.

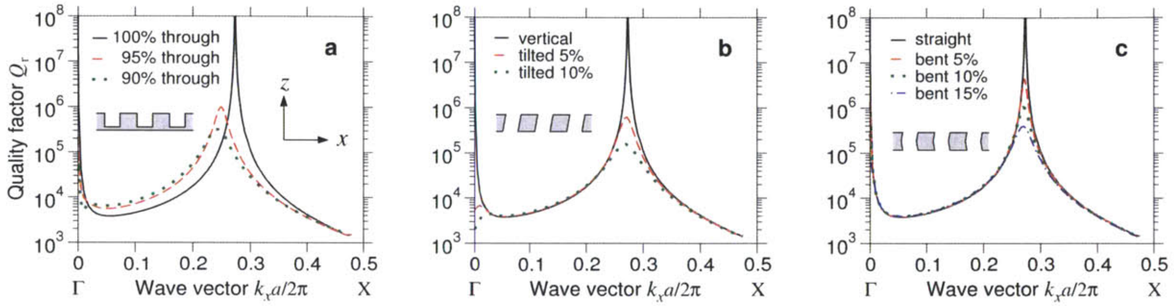

Figure 4-6: Quantitative evidence on the disappearance of leakage. a,b, Normalized radiative lifetime Q_r extracted from the experimentally-measured reflectivity spectrum (a) and the RCWA-calculated reflectivity spectrum (b). Black solid line shows prediction from FDTD.

4.6 Concluding remarks

In this chapter, we have observed an optical state that remains perfectly confined even though there exist symmetry-compatible radiation modes in its close vicinity; this realizes the long sought-after idea of trapping waves within the radiation continuum, without symmetry incompatibility [15–23, 78, 80]. The state has a high quality factor (implying low loss and large field enhancement), large area, and strong confinement near the surface, making it potentially useful for chemical/biological sensing, organic light emitting devices, and large-area laser applications. It also has wavevector and wavelength selectivity, making it suitable for optical filters, modulators, and waveguides. Furthermore, the ability to tune the maximal radiative Q_r from infinite to finite (Fig. 4-6) is another unique property that may be exploited. Lastly, the fundamental principles of this state hold for any linear wave phenomenon, not just optics.

Chapter 5

Topological Nature of BICs and a Unifying Theory

5.1 Introduction

In previous chapters, we have introduced the concept of bound states in the continuum (BICs) through a few examples. BICs are unusual solutions of wave equations describing light or matter: they are discrete and spatially bounded, but exist at the same energy as a continuum of states which propagate to infinity. Until recently, BICs were constructed through fine-tuning parameters in the wave equation [16, 80, 83–85] or exploiting the separability of the wave equation due to symmetry [51, 77, 86] as discussed in Chapter 2 and 3. More recently, BICs that that are both robust and not symmetry-protected ("accidental") have been predicted [2, 19, 21, 78, 87] and experimentally realized [2] in periodic structures; the simplest such system is a periodic dielectric slab [2] as discussed in Chapter 4. Their existence does not require fine-tuning of system parameters; small changes in parameters simply shift the position of these special points along the band diagram. An intuitive understanding of why such BICs exist and are robust was previously lacking. Recently, an explanation based on accidental triangular symmetry of the radiating fields was proposed [88] but does not explain the robustness of these BICs and their occurrences in TE-like bands.

In this chapter, we explore the fundamental nature of BICs and show that both types of BICs in such systems are vortex centers in the polarization direction of far-field radiation. The robustness of these BICs is due to the existence of conserved and quantized topological charges, defined by the number of times the polarization vectors wind around the vortex centers. Such charges can only be generated or annihilated by making large changes in the system parameters, and then only according to strict rules, which we derive and test numerically. Our results imply that laser emission based on such states will generate vector beams [89].

5.2 Basic nature of BICs

We now show that both types of BICs in photonic crystal slabs are vortex centers in the polarization direction of the far-field radiation of the slabs. Using the Bloch theorem for photonic crystals [3], we write the electric field of a resonance as $\mathbf{E}_{\mathbf{k}}(\boldsymbol{\rho}, z) = e^{i\mathbf{k}\cdot\boldsymbol{\rho}}\mathbf{u}_{\mathbf{k}}(\boldsymbol{\rho}, z)$, where $\mathbf{k} = k_x\hat{x} + k_y\hat{y}$ is the two-dimensional wave vector, $\boldsymbol{\rho} = x\hat{x} + y\hat{y}$ is the in-plane coordinate, $\mathbf{u}_{\mathbf{k}}$ is a periodic function in $\boldsymbol{\rho}$, and z is the normal direction to the slab. While the fields inside the slab are periodically modulated, outside the slab each state consists of propagating plane waves and/or evanescent waves that decay exponentially away from the surface. For states above the light line (resonances), and wavelengths below the diffraction limit, the only non-zero propagating-wave amplitudes are the zero-order (constant in-plane) Fourier coefficients of $\mathbf{u}_{\mathbf{k}}$, given by $\mathbf{c}(\mathbf{k}) = c_x(\mathbf{k})\hat{x} + c_y(\mathbf{k})\hat{y}$ (Fig. 5-1). Here, $c_x(\mathbf{k}) = \hat{x} \cdot \langle \mathbf{u}_{\mathbf{k}} \rangle$, $c_y(\mathbf{k}) = \hat{y} \cdot \langle \mathbf{u}_{\mathbf{k}} \rangle$, and the brackets denote spatial average over one unit cell on any horizontal plane outside the slab. Note that $\mathbf{c}(\mathbf{k})$ is the projection of $\langle \mathbf{u}_{\mathbf{k}} \rangle$ onto the xy plane; it points in the polarization direction of the resonance in the far field, so we refer to $\mathbf{c}(\mathbf{k})$ as the "polarization vector".

A resonance turns into a BIC when the outgoing power is zero, which happens if and only if $c_x = c_y = 0$. In general, c_x and c_y are both complex functions of $\mathbf{k}$, and varying the wave vector components (k_x, k_y) is not sufficient to guarantee a solution where $c_x = c_y = 0$. However, when the system is invariant under the operation $C_2^z T$, implying that $\epsilon(x, y, z) = \epsilon^*(-x, -y, z)$, we show that c_x and c_y can be chosen to be

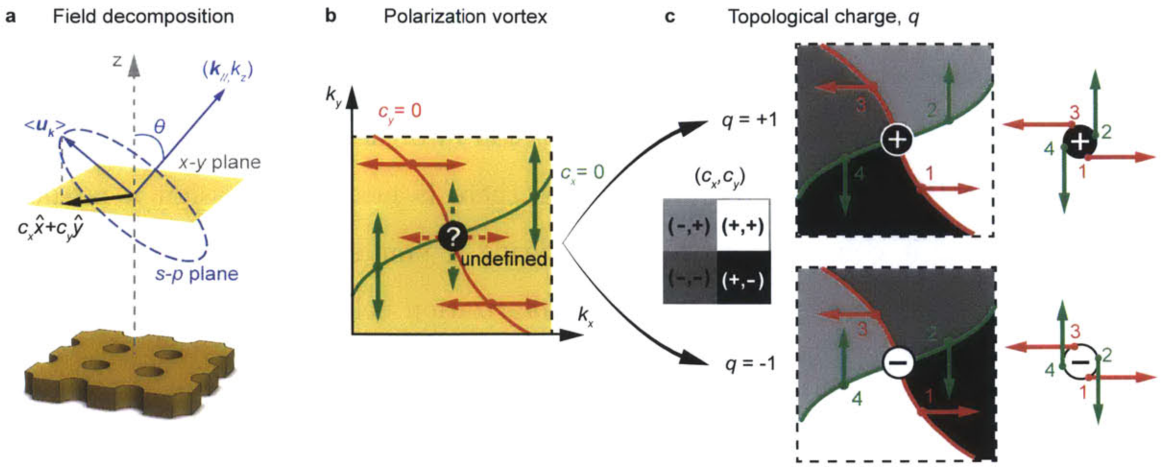

Figure 5-1: Stable bound states in the continuum (BICs) as vortex centers of polarization vectors. a, Schematics of radiation field decomposition for resonances of a slab structure. The spatially-averaged Bloch part of the electric field $\langle \boldsymbol{u_k} \rangle$ is projected onto the x-y plane as the polarization vector $\boldsymbol{c} = (c_x, c_y)$. A resonance turns into a BIC if and only if $c_x = c_y = 0$. b, Schematic illustration for the nodal lines of c_x (green) and of c_y (red) in a region of $\mathbf{k}$ space near a BIC. The direction of vector $\boldsymbol{c}$ (shown in arrows) becomes undefined at the nodal line crossing, where a BIC is found. c, Two possible configurations of the polarization field near a BIC. Along a closed loop in k-space containing a BIC (loop goes in counterclockwise direction, 1→2→3→4), the polarization vector either rotates by angle 2π (denoted by topological charge $q = +1$) or rotates by angle -2π (denoted by topological charge $q = -1$). Different regions of the k space are colored in four gray-scale colors according to the signs of c_x and c_y. In this way, a BIC happens where all four gray-scale colors meet, and charge $q = +1$ corresponds to the color changing from white to black along the counterclockwise loop C, and charge $q = -1$ corresponds to the color changing from black to white.

real numbers simultaneously; in other words, the far field is linearly polarized (see to the next section, here C_2^z is 180° rotation operator around z axis, and T is the time reversal operator). When the system also has up-down mirror symmetry (σ_z), the outgoing waves on one side of the slab determine those on the other; for such systems, BICs are stable because they correspond to the intersections between the nodal line of c_x and the nodal line of c_y in the k_x-k_y plane. Such a nodal intersection naturally causes a vortex in the polarization vector field centered on the BIC, as illustrated in Fig. 5-1 (b), for the simplest case. Along the nodal line of c_x (or c_y), the direction of $\mathbf{c}(\mathbf{k})$ is along the y axis (or x axis), as illustrated in Fig. 5-1b. As one encircles the nodal intersection (BIC) in the k_x-k_y plane each component of the polarization vector flips sign as its nodal line is crossed so as to create a net circulation of $\pm 2\pi$ in the polarization field. At the nodal intersection the polarization direction becomes undefined, since at the BIC there is zero emission into the far-field. Conversely one could say that BICs cannot radiate because there is no way to assign a far-field polarization that is consistent with neighbouring $\mathbf{k}$ points. Thus robust BICs are only possible when there is vorticity in the polarization field.

Vortices are characterized by their topological charges. Here, the topological charge (q) carried by a BIC is defined as:

$$q = \frac{1}{2\pi} \oint_C d\mathbf{k} \cdot \nabla_{\mathbf{k}} \phi(\mathbf{k}), \quad q \in \mathcal{Z} \tag{5.1}$$

which describes how many times the polarization vector winds around the BIC. Here, $\phi(\mathbf{k}) = \arg[c_x(\mathbf{k}) + ic_y(\mathbf{k})]$ is the angle of the polarization vector, and C is a closed simple path in k space that goes around the BIC in the counterclockwise direction.The fields $\mathbf{u_k}$ are chosen to be smooth functions of $\mathbf{k}$, so $\phi(\mathbf{k})$ is differentiable in $\mathbf{k}$ along the path. The polarization vector has to come back to itself after the closed loop, so the overall angle change must be an integer multiple of 2π, and q must be an integer. Fig. 1c shows examples of how the polarization vector winds around a BIC with charge $q = +1$ and also around a BIC with charge $q = -1$ along a loop C marked by 1→2→3→4→1. Similar definitions of winding numbers as in Eq. (5.1) can be found in describing topological defects [90] of continuous two-dimensional spins, dislocations in crystals, and quantized vortices in helium II [91]. This formalism describing polarization vortices is also closely related to Berry phases in describing adiabatic changes of polarization of light [92] and Dirac cones in gaphenes [93].

The far-field pattern at a definite $\mathbf{k}$ point by itself does not reflect the vorticity of polarization around a BIC, but laser emission centered on such a BIC will. Laser emission always has a finite width in k-space and this wave-packet will be centered on the BIC; hence it will consist of a superposition of plane waves from the neighborhood of the BIC, leading naturally to a spatial twist in the polarization for the outgoing beam. Such beams have been studied previously, and are known as vector beams [89], although their connection with BICs does not appear to have been realized. The number of twists in the polarization direction is known as the order number of the vector beam, and we now see that it is given by the topological charge carried by the BIC.

In the example of Fig. 5-2, we show the topological charges of BICs for a structure that has been experimentally realized in ref. 2. In this example, there are five BICs on the lowest-frequency TM-like band (Fig. 5-2(a)). We obtain polarization vectors $\mathbf{c}(\mathbf{k})$ from finite-difference time-domain (FDTD) calculations, which reveal five vortices with topological charges of ±1 at these five k points (Fig. 5-2(b)). As discussed above, the BICs and their topological charges can also be identified from the nodal-line crossings and the gray-scale colors of c_x and c_y (Fig. 5-2(c)).

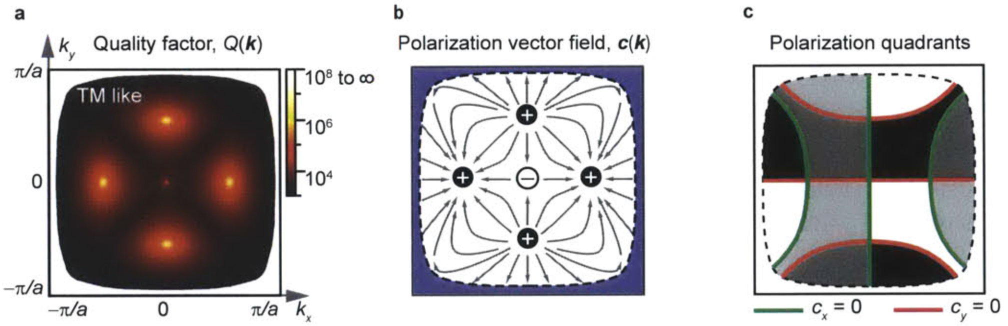

Figure 5-2: Characterization of BICs using topological charges. a, Calculated radiative quality factor Q of the TM_1 band on a square-lattice photonic crystal slab (as in ref. 2), plotted in the first Brillouin zone. Five BICs can be seen. b, Directions of the polarization vector field reveal vortices with topological charges of ±1 at each of the five k points. The area shaded in blue indicates modes below the lightline and thus bounded by total internal reflection. c, Nodal lines and gray-scale colors of the polarization vector fields (same coloring scheme as in Fig. 5-1 (c)).

5.3 Symmetry requirements for stable BICs

Here, we give the proof that stable BICs at arbitrary k points can be found when the system is invariant under $C_2^z T$ and σ_z operators, and that stable BICs at C_2^z-invariant k points can be found when the system has C_2^z symmetry. Here, C_2^z means 180° rotation around z axis, and T means the time reversal operator. The schematics of the symmetry requirement is summarized in Fig. 5-3.

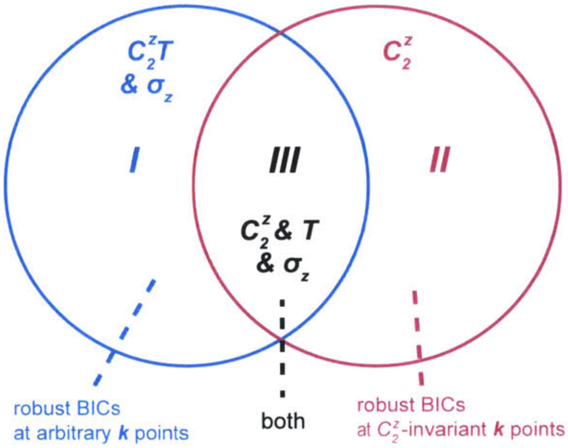

Figure 5-3: Symmetry requirements for BICs. Systems in the blue circle are invariant under operators C_2^zT and σ_z, where stable BICs at arbitrary wavevectors can be found. In the red circle, where C_2^z is a symmetry of the system, robust BICs can be found at high-symmetry wavevector points. Here, high-symmetry wavevectors mean C_2^z-invariant ones, while arbitrary wavectors are not necessarily C_2^z-invariant. In the overlapping area (region *III*), both types BICs can be found. All numerical examples in this Letter are within region *III*.

In region *I*, systems are invariant under the symmetry operator C_2^zT, namely $\epsilon^\star(x,y,z) = \epsilon(-x,-y,z)$. Let $\mathbf{u_k}$ be an eigenfunction of the master operator [3] $\Theta_\mathbf{k} = \frac{1}{\epsilon}(\nabla + i\mathbf{k}) \times (\nabla + i\mathbf{k})\times$, and recall that $\mathbf{k}$ here only has x and y components since we are considering a slab structure that does not have translational symmetry in z. A short derivation shows that at any $\mathbf{k}$ point, $\mathbf{u_k}(\mathbf{r})$ and $C_2^z\mathbf{u}_\mathbf{k}^*(C_2^z\mathbf{r})$ are both eigenfunctions of $\Theta_\mathbf{k}(\mathbf{r})$ with the same eigenvalue, so they must differ at most by a phase factor,

$$\begin{aligned} \mathbf{u_k}(\mathbf{r}) &= e^{i\theta_\mathbf{k}} C_2^z \mathbf{u}_\mathbf{k}^*(C_2^z\mathbf{r}) \\ &= e^{i\theta_\mathbf{k}}(-\mathbf{u}_\mathbf{k}^{x*}, -\mathbf{u}_\mathbf{k}^{y*}, \mathbf{u}_\mathbf{k}^{z*})|_{(-x,-y,z)} \end{aligned} \tag{5.2}$$

Here $\theta_\mathbf{k}$ is an arbitrary phase factor. Meanwhile, we are free to multiply $\mathbf{u_k}$ with any phase factor, and it remains a valid eigenfunction. For our purpose here, we explicitly choose the phase factor of $\mathbf{u_k}$ such that $e^{i\theta_\mathbf{k}} = -1$ for all $\mathbf{k}$. With this choice, we can average over x and y to get $\mathbf{c}(\mathbf{k}) = \mathbf{c}^*(\mathbf{k})$ for all $\mathbf{k}$. That is, the polarization vector $\mathbf{c}(\mathbf{k})$ is purely real.

Using the fact that systems in region I also have the up-down mirror symmetry σ_z, namely $\epsilon(x, y, z) = \epsilon(x, y, -z)$, we can link the radiation loss above and below the photonic crystal slab denoted by $\mathbf{c}^\uparrow$ and $\mathbf{c}^\downarrow$. At any $\mathbf{k}$ point, $\mathbf{u_k}(\mathbf{r})$ and $\sigma_z\mathbf{u_k}(\sigma_z\mathbf{r})$ are both eigenfunctions of $\Theta_\mathbf{k}(\mathbf{r})$ with the same eigenvalue, so

$$\begin{aligned} \mathbf{u_k}(\mathbf{r}) &= e^{i\theta_\mathbf{k}}\sigma_z\mathbf{u_k}(\sigma_z\mathbf{r}) \\ &= e^{i\theta_\mathbf{k}}(\mathbf{u}^x_\mathbf{k}, \mathbf{u}^y_\mathbf{k}, -\mathbf{u}^z_\mathbf{k})|_{(x,y,-z)} \end{aligned} \tag{5.3}$$

with $\theta_\mathbf{k}$ being an arbitrary phase factor (not to be confused with the one in Eq. (5.2)). Since $\sigma_z^2 = 1$, we can apply Eq. (5.3) twice to show that $e^{i\theta_\mathbf{k}} = \pm 1$. Averaging over x and y, we see that $\mathbf{c}^\uparrow = \pm\mathbf{c}^\downarrow$.

After using these two symmetries, the number of independent real variables in all radiation coefficients $c^{\uparrow,\downarrow}_{x,y}$ has been reduced from 8 to 2. Given that the number of independent tuning parameters is also 2: (k_x, k_y), we are able to get stable BICs. Note that the combination of C_2^zT and σ_z is just one sufficient condition for stable BICs in photonic crystal slabs. There might be other different choices of symmetries. For example, PT and σ_z is equivalent to C_2^zT and σ_z, where P is the inversion operator. Also, the requirement of σ_z is not necessary when there is leakage to one direction only (such as BICs on the surface of a photonic bandgap structure [78]).

In region *II*, stable BICs at C_2^z-invariant k points can be found. Systems in this region have C_2^z symmetry, namely $\epsilon(x, y, z) = \epsilon(-x, -y, z)$. k points are C_2^z-invariant when $-\mathbf{k} = \mathbf{k} + \mathbf{G}$, with $\mathbf{G}$ being a reciprocal lattice vector. A short derivation shows that at any k point, $\mathbf{u_k}(\mathbf{r})$ and $C_2^z\mathbf{u}_{-\mathbf{k}}(C_2^z\mathbf{r})$ are both eigenfunctions of $\Theta_\mathbf{k}(\mathbf{r})$ with the same eigenvalue, so

$$\mathbf{u_k}(\mathbf{r}) = e^{i\theta_\mathbf{k}}C_2^z\mathbf{u}_{-\mathbf{k}}(C_2^z\mathbf{r}), \tag{5.4}$$

with $\theta_\mathbf{k}$ being an arbitrary phase factor (not to be confused with the two phase factors above). At these high-symmetry $\mathbf{k}$ points, using Bloch theorem we know: $\mathbf{u}_{-\mathbf{k}} = \mathbf{u}_{\mathbf{k}+\mathbf{G}} = \mathbf{u_k}$, so we can apply Eq. (5.4) twice to get $e^{i\theta_\mathbf{k}} = \pm 1$. When this factor is $+1$, we can average over x and y to see that $\mathbf{c}(\mathbf{k}) = 0$, corresponding to a BIC at this C_2^z-invariant k point.

In region *III*, both kinds of BICs can be found, where C_2^z, T and σ_z are all present. All our numerical examples are within this region to make it easier to understand the relation and interaction between different types of BICs.

5.4 Conservation rules of topological charges

The winding number of polarization vector along a closed path is given by the sum of the topological charges carried by all BICs enclosed within this path [90]. When system parameters vary continuously, the winding number defined on this path remains invariant, unless there are BICs crossing the boundary. Therefore, topological charge is a conserved quantity. This conservation rule leads to consequences/restrictions on behaviors of the BICs. For example, as long as the system retains C_2^zT and σ_z symmetries, a BIC can only be destroyed through annihilation with another BIC of the exact opposite charge, or through bringing it outside of the continuum (below the light line).

Since topological charge is a conserved quantity, there are a few consequences and restriction on the evolution of BICs. First, BICs are stable as long as the system retains required symmetries; however, perturbations that break these two required symmetries eliminate the existence of BICs. When C_2^zT symmetry is broken, the coefficients (c_x and c_y) require complex components, meaning the radiation becomes elliptically polarized instead of linearly polarized. When σ_z symmetry is broken, the coefficients $c_{x,y}^{\uparrow,\downarrow}$ are still real numbers, but radiation towards the top and towards the bottom become separate degrees of freedom and so they do not vanish simultaneously in general. Second, when BICs collide into each other in the moment space, the sum of all topological charges they carry remains the same before and after the collision.

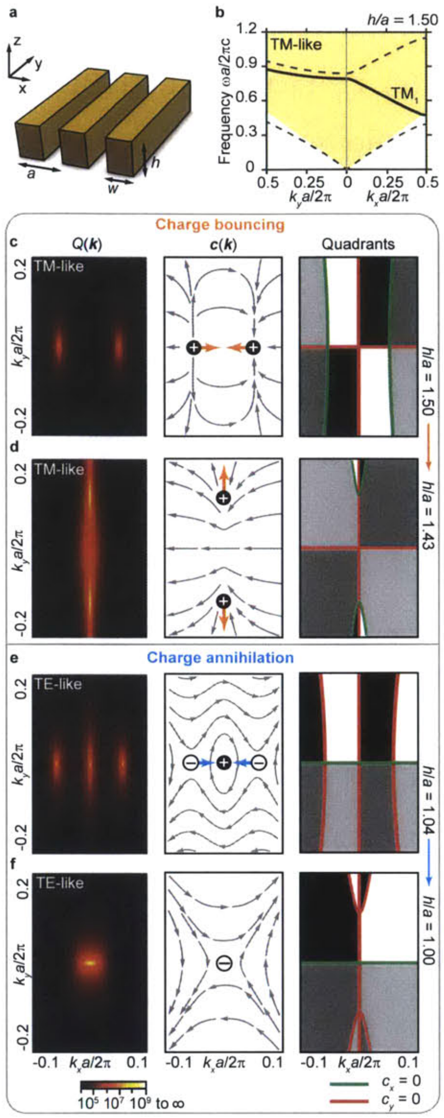

Figure 5-4: Evolution of BICs and conservation of topological charges.

5.4.1 Evolution of BICs

The conservation of topological charges allows us to predict and understand the behaviors of BICs when the parameters of the system are varied over a wide range, as we now illustrate. First, consider the lowest-frequency TM-like mode (TM_1 band) of a 1D-periodic structure in air shown in Fig. 5-4 (a). This grating consists of a periodic array of dielectric bars with periodicity of a, width $w = 0.45a$, and refractive index $n = 1.45$. Its calculated band structure is shown in Fig. 5-4 (b). When the thickness of the grating is $h = 1.50a$, there are two BICs on the k_x axis, as indicated by the radiative quality factor of the resonances (Fig. 5-4 (c)). The polarization vector $\mathbf{c}(\mathbf{k})$, also shown in Fig. 5-4 (c), characterizes both BICs as carrying charges $q = +1$. When the grating thickness is decreased to $h/a = 1.43$ (all other parameters fixed), the two BICs move towards the center of the Brillouin zone, meet at the $\mathbf{\Gamma}$ point, and deflect onto the k_y axis (Fig. 5-4 (d)). This is inevitable due to the conservation of the topological charges: annihilation cannot happen between two BICs of the same charge.

5.4.2 Annihilation of BICs

Annihilation of BICs is only possible when charges of opposite signs are present. This can be seen in the lowest-frequency TE-like band of the same structure (Fig. 5-4 (e),(f)). When $h/a = 1.04$, there are two off-$\mathbf{\Gamma}$ BICs with charge -1 and a BIC with charge $+1$ at the $\mathbf{\Gamma}$ point (Fig. 5-4 (e)). As h/a decreases, the two -1 charges move to the center and eventually annihilate with the $+1$ charge, leaving only one BIC with charge $q = -1$ (Fig. 5-4 (f)).

5.4.3 Generation of BICs

Generation of BICs is also restricted by charge conservation, and can be understood as the reverse process of annihilation. We provide an example by considering the lowest-frequency TE-like mode in a photonic crystal slab of $n = 3.6$ with a square lattice of cylindrical air holes of diameter $d = 0.5a$ (Fig. 5-5 (a)). As the slab thickness increases, BICs are generated at the $\mathbf{\Gamma}$ point. Each time, four pairs of BICs with exact opposite charges are generated, consistent with charge conservation and C_{4v} symmetry of the structure. With further increase of the slab thickness, the eight BICs move outward along high-symmetry lines and eventually go outside of the continuum (fall below the light line).

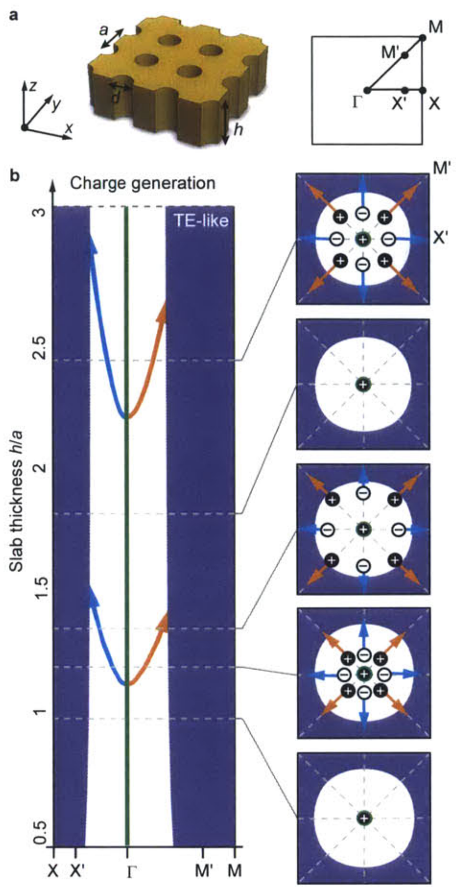

Figure 5-5: Generation of BICs. a, Schematic drawing of a photonic crystal slab with two-dimensional periodicity. b, Generation of BICs on the TE_1 band when the slab thickness h is increased. Each time, four pairs of BICs with charges ± 1 are generated simultaneously, consistent with the charge conservation and C_{4v} symmetry. Insets show the locations of BICs in the k space and their corresponding topological charges for $h/a = 1.0, 1.2, 1.35, 1.8$, and 2.4. As the slab thickness increases, the BICs move outward and eventually fall below the light line into the area shaded in dark blue.

5.5 Constraints from system symmetries on BICs

When system has certain symmetries, the master equation usually will share the same symmetries, which leads to constraints on the band structures and mode profiles. Furthermore, we show that these system symmetries also lead to constraints on the occurance of BICs and the topological charges they carry.

In particular, in this section, we will show: 1. all BICs related by point group symmetries (rotations and reflections) must carry the same topological charges; 2. BICs at high-symmetry k points can only carry certain topological charges, depending on the detailed mode profiles. As an example, we will focus on allowed topological charges allowed at Γ point of systems with different symmetries.

5.5.1 BICs related by system symmetires carry the same topological charge

Here, we prove that when the structure has a certain in-plane point group symmetry $\mathcal{R}$ (namely, $\epsilon(\mathbf{r}) = \epsilon(\mathcal{R}\mathbf{r})$; $\mathcal{R}$ can be a combination of rotation and reflection on the x-y plane) and when the band has no degeneracy, a BIC at $\mathbf{k}$ indicates there is another BIC at $\mathcal{R}\mathbf{k}$ with the same topological charge. The assumption here is that the eigenfunctions $\mathbf{u}_\mathbf{k}$ at different k points already have their phases chosen to ensure the reality of $\mathbf{c}(\mathbf{k})$, and the signs of $\mathbf{u}_\mathbf{k}$ at different k points have been chosen such that $\mathbf{u}_\mathbf{k}$ is continuous with respect to $\mathbf{k}$ (so that a small change in $\mathbf{k}$ leads to a small change in $\mathbf{u}_\mathbf{k}$).

We start by relating the eigenfunction at $\mathbf{k}$ and the eigenfunction at $\mathcal{R}\mathbf{k}$. Let $\mathbf{u}_\mathbf{k}$ be an eigenfunction of operator $\Theta_\mathbf{k}$. Since the system is invariant under transformation $\mathcal{R}$, we know $\hat{O}_\mathcal{R}\mathbf{u}_\mathbf{k}$ is an eigenfunction of $\Theta_{\mathcal{R}\mathbf{k}}$, so in the absence of degeneracy, we can write $\hat{O}_\mathcal{R}\mathbf{u}_\mathbf{k} = \alpha_\mathbf{k}\mathbf{u}_{\mathcal{R}\mathbf{k}}$, where $\alpha_\mathbf{k}$ is some number. The number $\alpha_\mathbf{k}$ must have unit magnitude (due to the normalization of $\mathbf{u}_\mathbf{k}$ and $\mathbf{u}_{\mathcal{R}\mathbf{k}}$) and must be real-valued (because $\mathbf{c}(\mathbf{k})$ is real-valued), so it can only take on discrete values of ± 1. Also, $\alpha_\mathbf{k}$ must be a continuous function of $\mathbf{k}$ since $\mathbf{u}_\mathbf{k}$ is continuous with respect to $\mathbf{k}$. Since $\alpha_\mathbf{k}$ is both discrete-valued and continuous, it must be a constant. Then, we may denote this constant with its value at the Γ point, as $\alpha_\mathbf{k} = \alpha_\Gamma$. Note that $\mathcal{R}\mathbf{\Gamma} = \mathbf{\Gamma}$, so we can determine coefficient $\alpha_\mathbf{\Gamma}$ using the mode profile: $\hat{O}_\mathcal{R}\mathbf{u}_\mathbf{\Gamma} = \alpha_\mathbf{\Gamma}\mathbf{u}_\mathbf{\Gamma}$. In conclusion, we have $\mathbf{u}_{\mathcal{R}\mathbf{k}} = \alpha_\Gamma\hat{O}_\mathcal{R}\mathbf{u}_\mathbf{k}$.

Now we consider how the angle $\phi(\mathcal{R}\mathbf{k})$ is related to $\phi(\mathbf{k})$. The vector field $\mathbf{u}_\mathbf{k}$ transforms under the rotation operator as $(\hat{O}_\mathcal{R}\mathbf{u}_\mathbf{k})(\mathbf{r}) = \mathcal{R}\mathbf{u}_\mathbf{k}(\mathcal{R}^{-1}\mathbf{r})$, so averaging over x and y we get $\langle\hat{O}_\mathcal{R}\mathbf{u}_\mathbf{k}\rangle = \mathcal{R}\langle\mathbf{u}_\mathbf{k}\rangle$. Let P be the operator that projects a 3D vector onto the x-y plane, namely $P\mathbf{r} = \mathbf{r} - (\mathbf{r}\cdot\hat{z})\hat{z}$; it commutes with $\mathcal{R}$, since it does not alter the x or y component. Then $\mathbf{c}(\mathbf{k}) = P\langle\mathbf{u}_\mathbf{k}\rangle$, and

$$\mathbf{c}(\mathcal{R}\mathbf{k}) = P\langle\mathbf{u}_{\mathcal{R}\mathbf{k}}\rangle = P\langle\alpha_\Gamma \hat{O}_\mathcal{R}\mathbf{u}_\mathbf{k}\rangle = \alpha_\Gamma \mathcal{R} P\langle\mathbf{u}_\mathbf{k}\rangle = \alpha_\Gamma \mathcal{R}\mathbf{c}(\mathbf{k}). \tag{5.5}$$

So, the polarization vector at the the transformed k point is simply the original polarization vector transformed and times ±1. So, the angle of the polarization vector only changes by a constant in the case of proper rotations (where $\det\mathcal{R} = 1$); in the case of improper rotations (where $\det\mathcal{R} = -1$), it also changes sign. So, in general, we can write

$$\phi(\mathcal{R}\mathbf{k}) = (\det\mathcal{R})\phi(\mathbf{k}) + c \tag{5.6}$$

with c being a constant depending on $\mathcal{R}$ and α_Γ. It follows that $\nabla_{\mathcal{R}\mathbf{k}}\phi(\mathcal{R}\mathbf{k}) = (\det\mathcal{R})\mathcal{R}\nabla_\mathbf{k}\phi(\mathbf{k})$, so the topological charge at $\mathcal{R}\mathbf{k}$ is

$$\begin{aligned}
q_{\mathcal{R}\mathbf{k}} &= \frac{1}{2\pi}\oint_{C_{\mathcal{R}\mathbf{k}}} \nabla_{\mathbf{k}''}\phi(\mathbf{k}'')\cdot d\mathbf{k}'' && (5.7)\\
&= \frac{1}{2\pi}\oint_{\mathcal{R}^{-1}C_{\mathcal{R}\mathbf{k}}} \nabla_{\mathcal{R}\mathbf{k}'}\phi(\mathcal{R}\mathbf{k}')\cdot \mathcal{R}d\mathbf{k}' && (5.8)\\
&= \frac{1}{2\pi}(\det\mathcal{R})\oint_{C_\mathbf{k}} \nabla_{\mathcal{R}\mathbf{k}'}\phi(\mathcal{R}\mathbf{k}')\cdot \mathcal{R}d\mathbf{k}' && (5.9)\\
&= \frac{1}{2\pi}(\det\mathcal{R})^2\oint_{C_\mathbf{k}} \mathcal{R}\nabla_{\mathbf{k}'}\phi(\mathbf{k}')\cdot \mathcal{R}d\mathbf{k}' && (5.10)\\
&= \frac{1}{2\pi}\oint_{C_\mathbf{k}} \nabla_{\mathbf{k}'}\phi(\mathbf{k}')\cdot d\mathbf{k}' && (5.11)\\
&= q_\mathbf{k}, && (5.12)
\end{aligned}$$

where $C_{\mathcal{R}\mathbf{k}}$ is a closed simple path that is centered on $\mathcal{R}\mathbf{k}$ and loops in counterclockwise direction, $\mathcal{R}^{-1}C_{\mathcal{R}\mathbf{k}}$ is this loop transformed by $\mathcal{R}^{-1}$ (which centers on $\mathbf{k}$ in counterclockwise direction if $\mathcal{R}$ is a proper rotation, or in clockwise direction if $\mathcal{R}$ is improper), and $C_\mathbf{k}$ is this transformed loop traversed in counterclockwise direction.

In conclusion, we have proven that if a system has certain point group symmetry $\mathcal{R}$, then the topological charges carried by the BIC at $\mathbf{k}$ and at $\mathcal{R}\mathbf{k}$ on a singly degenerate band have to be the same. This conclusion agrees with all examples in Figs. 5-2-5-5.

5.5.2 Allowed charges at Γ in systems with different symmetries

Although the examples discussed so far only show topological charges of ±1, other values of charges can be found in higher-frequency bands of the PC or in structures with higher rotational symmetry. For example, Fig. 5-6 shows a stable BIC of charge -2 at the $\mathbf{\Gamma}$ point arising from the double degeneracy of nodal lines caused by the C_{6v} symmetry of the system.

The symmetries of the system also restrict the possible values of topological charges, since the nodal curves must respect the point symmetry. Following similar derivation as in the previous section, one can calculate all possible topological charges of BICs at high symmetry $\mathbf{k}$ points. For a system with C_n symmetry, the possible topological charges at the Γ point on a singly-degenerate band are given in Table 5.1. This is consistent with all examples in this paper. This table can be used to predict the charges in other systems of interest and to design high order vector beams.

Table 5.1: Allowed stable topological charges at Γ for singly degenerate bands. $A(B)$ corresponds to modes of different representations of the symmetry operator [70]. Note that only singly degenerate representations of symmetry operators are included in here.

Symmetries representation	Charges	Allowed n	Allowed charges
A mode of C_2	$\pm 1 + 2n$	0	±1
B mode of C_2	$0 + 2n$	0	0
A mode of C_3	$1 + 3n$	$0, \pm 1...$	+1,+4,-2,...
A mode of C_4	$1 + 4n$	$0, \pm 1, ...$	+1,+5,-3,...
B mode of C_4	$-1 + 4n$	$0, \pm 1, ...$	-1,-5,+3,...
A mode of C_6	$1 + 6n$	$0, \pm 1, ...$	+1,+7,-5,...
B mode of C_6	$-2 + 6n$	$0, \pm 1, ...$	-2,+4,-8,...

Allowed topological charges at high symmetry k points can be determined by the field eigenvalues of the rotational symmetry of a system. For systems with m-fold rotational symmetry, we can first determine the relationship between polarization direction at wavevector $\mathbf{k}$ and at rotated wavevector $\mathcal{R}\mathbf{k}$ ($\phi(\mathbf{k})$ and $\phi(\mathcal{R}\mathbf{k})$) using Eq. (5.5). Since the wavevector gets back to its original point if applying this rotation

m-times: $\mathcal{R}^m\mathbf{k} = \mathbf{k}$, we can then apply this relationship m times and get how many times the polarization vector rotates around the center of the Brillouin zone. From there, we categoraize all possible charges allowed at $\mathbf{\Gamma}$ as shown in Table S1. Allowed charges depend on two factors. The first one is which symmetry representation the band belongs to. The second one is the degeneracy of nodal lines at Γ, because more nodal lines intersecting at the same point usually leads to more oscillations in color and thus higher topological charges. This factor is reflected by the integer number n, depending on the number of equivalent $\mathbf{\Gamma}$ points at this frequency [94]. Note that only singly degenerate bands are considered here, having no crossing with other bands in the bandstructures, as can be seen in Table 5.1. Further research directions may include BICs on degenerate bands, as well as the search of BICs with higher-order and potentially fractional topological charges. Also, it is worth exploring the behavior of BICs (topological charges) happening at crossing bands. One speculative prediction is that: they might be able to hop from one band to the other through the crossing of the bands. Finally, it is interesting to explore whether the location of BICs may coincide with Dirac points. As is known: optical Dirac points only happen below the light lines, and thus are always true eigenmodes with infinitely long lifetime. When radiation losses are introduced, the Dirac points normally break up into separate bands. However, there is no radiation loss at BICs, therefore it is possible to find optical Dirac point beyond lightline with the help of BICs.

5.5.3 Example of charge -2

Although the examples discussed so far only show topological charges of ±1, other values of charges can be found in higher-frequency bands of the PC or in structures with higher rotational symmetry. For example, Fig. 5-6 shows a stable BIC of charge -2 at the $\mathbf{\Gamma}$ point arising from the double degeneracy of nodal lines caused by the C_{6v} symmetry of the system. We consider the lowest-frequency TE-like mode of a photonic crystal slab with a hexagonal lattice of cylindrical air holes (shown in Fig. 5-6(a)). The refractive index of the slab is $n = 1.5$; the air-hole diameter is $0.5a$; and the thickness of the slab is 0.5a, where a is the lattice constant. This system has C_6^z symmetry. Normalized lifetime plot indicates a BIC at the center of the Brillouin zone shown in Fig. 5-6(b). The polarization vector field characterizes the BIC carrying charge -2 shown in Fig. 5-6(c). Charge -2 can also be understood from the double degeneracy of both nodal lines of c_x (green) and c_y (red), shown in the inset of Fig. 5-6(c). All four nodal lines are pinned at Γ point stabilized by the C_6 symmetry.

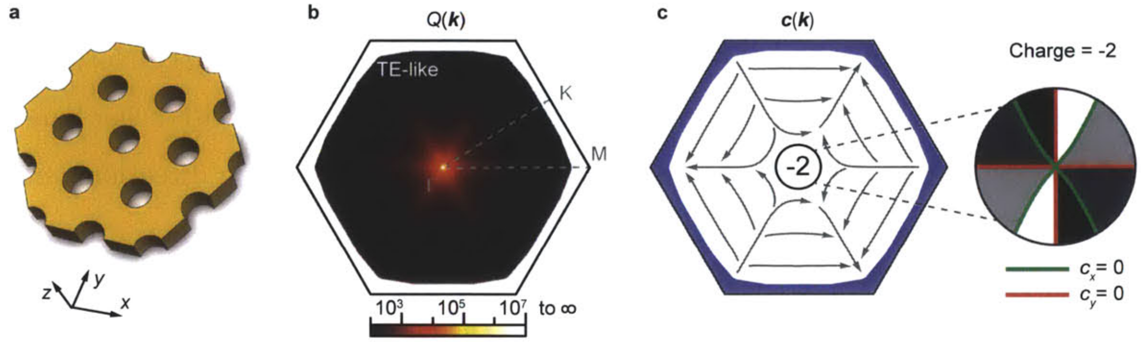

Figure 5-6: Stable BIC with topological charge -2. a, Schematic drawing of the photonic crystal slab. b, Q plotted in the first Brillouin zone, showing a BIC at the Γ point. c, Polarization vector field characterizes the BIC with a stable topological charge of -2, as can be shown from double degeneracies of both nodal lines.

5.6 Concluding remarks

We have demonstrated that BICs in photonic crystal slabs are associated with vortices in the polarization field and explained their robustness in terms of conserved topological charges. We derive the symmetries that constrain these charges and explain their generation, evolution and annihilation. We conjecture that all robust BICs [2, 19, 21, 51, 77, 78, 86, 87] will correspond to vortices in an appropriate parameter space. Our finding connects electromagnetic BICs to a wide range of physical phenomena including Berry phases around Dirac points [93], topological defects [90], and general vortex physics [91]. Optical BICs in photonic crystals have a wealth of applications. Lasing action can naturally occur at BIC states where the quality factor diverges. The angular (wavevector) tunablity of the BICs makes them great candidates for on-chip beam-steering [95]. Furthermore, photonic crystal lasers through

BICs are naturally vector beams [94, 96], which are important for particle accelerations, optical trapping and stimulated emission depletion microscopy.

Chapter 6

Conclusion

In this thesis, we study two types optical BICs from both theoretical and experimental aspects.

We first demonstrate the existence of the first type of optical BICs: the one protected by symmetry, in macroscopic photonic crystal slabs. When the wavevector approaches 0, the lifetime of the modes approaches infinity while living within the lightcone. Through fitting the angular reflectivity measurement results to a temporal coupled mode theory, we were able to extract the quality factor and demonstrate the existence of these special modes.

We then show that these BICs have prefound implication in light-emission applications from two aspects. First, they allow strong and tunable interaction between the modes and added organic molecules anywhere along the surface. Meanwhile, due to the existing enhancement mechanisms induced by the BICs, the lasing threshold of the system was reduced by an order of magnitude compared to demonstrated results.

Next, we demonstrate the existence of a completely different type of BICs: those are not due to symmetry mismatching. The explanation for these modes are through the simultaneous vanishing of radiation leakage through all channels. However, these modes exist in a robust way: when certain system parameters vary, they won't disapear, instead they simply shift to a different position in the wavevector space.

Finally, we show there is a unifying theory that explains the fundamental understanding of both types of BICs. They are all vortex centers of the polarization directions in the far field. We also give a topological explanation on the robustness of the BICs based on the topological orders they carry.

A few directions worth exploring in the future include the following:

1. To explore the existence of BICs and their robustness in systems that include gain and loss while maintaining *PT* symmetry. So far, all discussion are based on passive structures, meaning without any gain or loss. However, derivation in Chapter 5 shows BICs can exist in all *PT* symmetric systems. It is of interest to demonstrate their existence and study any possible "critical point" behaviors normally associated with *PT* symmetric systems.
2. To break the up-down mirror symmetry and design a laser that mostly radiate to the air. Most photonic crystal based lasers suffer from a common problem: most (or at least half) of the radiation come towards the high-index substrates instead of the air side. This leads to additional complicated and delicate designs for the bottom of these lasers to reflect this radiation with a specific phase shift. However, if we break the up-down mirror symmetry and design a system where the topological charge of polarization vector is much smaller on the air side than on the substrate side, then the radiation will naturally mostly towards the air side and therefore of great advantage.
3. To relate embedded eigenvalue problems to other seemingly related topics, like embedded solitons.

Bibliography

[1] Victor Liu and Shanhui Fan. S^4 : A free electromagnetic solver for layered periodic structures. *Comput. Phys. Commun.*, 183(10):2233 – 2244, 2012.

[2] Chia Wei Hsu, Bo Zhen, Jeongwon Lee, Song-Liang Chua, Steven G. Johnson, John D. Joannopoulos, and Marin Soljačić. Observation of trapped light within the radiation continuum. *Nature*, 499(7457):188–191, 07 2013.

[3] J. D. Joannopoulos, S. G. Johnson, J. N. Winn, and R. D. Meade. *Photonic Crystals: Molding the Flow of Light.* Princeton University Press, 2 edition, 2008.

[4] Oscar Painter, J Vučkovič, and Axel Scherer. Defect modes of a two-dimensional photonic crystal in an optically thin dielectric slab. *JOSA B*, 16(2):275–285, 1999.

[5] H.C.Y. Yamamoto and F. Tassone. *Semiconductor Cavity Quantum Electrodynamics.* Springer, 2000.

[6] Reginald K Lee, Yong Xu, and Amnon Yariv. Modified spontaneous emission from a two-dimensional photonic bandgap crystal slab. *JOSA B*, 17(8):1438–1442, 2000.

[7] Alexei A Erchak, Daniel J Ripin, Shanhui Fan, Peter Rakich, John D Joannopoulos, Erich P Ippen, Gale S Petrich, and Leslie A Kolodziejski. Enhanced coupling to vertical radiation using a two-dimensional photonic crystal in a semiconductor light-emitting diode. *Applied Physics Letters*, 78(5):563–565, 2001.

[8] Susumu Noda, Mitsuru Yokoyama, Masahiro Imada, Alongkarn Chutinan, and Masamitsu Mochizuki. Polarization mode control of two-dimensional photonic crystal laser by unit cell structure design. *Science*, 293(5532):1123–1125, 2001.

[9] Masayuki Fujita, Shigeki Takahashi, Yoshinori Tanaka, Takashi Asano, and Susumu Noda. Simultaneous inhibition and redistribution of spontaneous light emission in photonic crystals. *Science*, 308(5726):1296–1298, 2005.

[10] A Rosenberg, Michael Carter, J Casey, Mijin Kim, Ronald Holm, Richard Henry, Charles Eddy, V Shamamian, K Bussmann, Shouyuan Shi, et al. Guided resonances in asymmetrical gan photonic crystal slabs observed in the visible spectrum. *Optics express*, 13(17):6564–6571, 2005.

[11] Susumu Noda, Masayuki Fujita, and Takashi Asano. Spontaneous-emission control by photonic crystals and nanocavities. *Nature photonics*, 1(8):449–458, 2007.

[12] Dirk Englund, A. Faraon, I. Fushman, S. Stoltz, P. Petroff, and Jelena Vučković. Controlling the spontaneous emission rate of single quantum dots in a two-dimensional photonic crystal. *Phys. Rev. Lett.*, 95:13904, 2005.

[13] M. Ghebrebrhan, Peter Bermel, Y. X. Yeng, Ivan Celanovic, Marin Soljačić, and J. D. Joannopoulos. *Phys. Rev. A*, 83:033810, 2011.

[14] Song-Liang Chua, Yidong Chong, A. Doug Stone, Marin Soljačić, and Jorge Bravo-Abad. Low-threshold lasing action in photonic crystal slabs enabled by fano resonances. *Opt. Express*, 19:1539–1562, 2011.

[15] Frank H. Stillinger and David R. Herrick. Bound states in the continuum. *Phys. Rev. A*, 11(2):446–454, Feb 1975.

[16] H. Friedrich and D. Wintgen. Interfering resonances and bound states in the continuum. *Phys. Rev. A*, 32(6):3231–3242, Dec 1985.

[17] J. M. Zhang, Daniel Braak, and Marcus Kollar. Bound states in the continuum realized in the one-dimensional two-particle hubbard model with an impurity. *Phys. Rev. Lett.*, 109(11):116405, Sep 2012.

[18] M. R. Watts, S. G. Johnson, H. A. Haus, and J. D. Joannopoulos. Electromagnetic cavity with arbitrary q and small modal volume without a complete photonic bandgap. *Opt. Lett.*, 27(20):1785–1787, Oct 2002.

[19] D. C. Marinica, A. G. Borisov, and S. V. Shabanov. Bound states in the continuum in photonics. *Phys. Rev. Lett.*, 100(18):183902, May 2008.

[20] Mario I. Molina, Andrey E. Miroshnichenko, and Yuri S. Kivshar. Surface bound states in the continuum. *Phys. Rev. Lett.*, 108(7):070401, Feb 2012.

[21] R. Porter and D.V. Evans. Embedded rayleigh-bloch surface waves along periodic rectangular arrays. *Wave Motion*, 43(1):29 – 50, 2005.

[22] C. M. Linton and P. McIver. Embedded trapped modes in water waves and acoustics. *Wave Motion*, 45:16, 2007.

[23] Helge Krüger. On the existence of embedded eigenvalues. *J. Math. Anal. Appl.*, 395(2):776, 2012.

[24] P. Paddon and Jeff F. Young. Two-dimensional vector-coupled-mode theory for textured planar waveguides. *Phys. Rev. B*, 61(3):2090–2101, Jan 2000.

[25] T. Ochiai and K. Sakoda. Dispersion relation and optical transmittance of a hexagonal photonic crystal slab. *Phys. Rev. B*, 63(12):125107, Mar 2001.

[26] Shanhui Fan and J. D. Joannopoulos. Analysis of guided resonances in photonic crystal slabs. *Phys. Rev. B*, 65(23):235112, Jun 2002.

[27] V. Pacradouni, W. J. Mandeville, A. R. Cowan, P. Paddon, Jeff F. Young, and S. R. Johnson. Photonic band structure of dielectric membranes periodically textured in two dimensions. *Phys. Rev. B*, 62(7):4204–4207, Aug 2000.

[28] Ehsan Shah Hosseini, Siva Yegnanarayanan, Mohammad Soltani, and Ali Adibi. Ultra-high quality factor microdisk resonators for chip-scale visible integrated photonics. In *Frontiers in Optics*, page FMG4. Optical Society of America, 2008.

[29] Ardavan F. Oskooi, David Roundy, Mihai Ibanescu, Peter Bermel, J. D. Joannopoulos, and Steven G. Johnson. Meep: A flexible free-software package for electromagnetic simulations by the fdtd method. *Comput. Phys. Commun.*, 181(3):687–702, 2010.

[30] JM Pottage, E Silvestre, and P St J Russell. Vertical-cavity surface-emitting resonances in photonic crystal films. *JOSA A*, 18(2):442–447, 2001.

[31] David Chan, Ivan Celanovic, J. D. Joannopoulos, and Marin Soljačić. Emulating one-dimensional resonant q-matching behavior in a two-dimensional system via fano resonances. *Phys. Rev. A*, 74:064901, 2006.

[32] V Donzella and F Crea. Optical biosensors to analyze novel biomarkers in oncology. *J Biophotonics*, 4:442–452, 2011.

[33] XD Hoa, AG Kirk AG, and M Tabrizian. Towards integrated and sensitive surface plasmon resonance biosensors: a review of recent progress. *Biosens Bioelectron*, 23:151–160, 2007.

[34] HK Hunt and AM Armani. Label-free biological and chemical sensors. *Nanoscale*, 2:1544–1559, 2010.

[35] MA Cooper. Optical biosensors in drug discovery. *Nat Rev Drug Discov*, 1:515–528, 2002.

[36] JR Lakowicz. *Principles of Fluorescence Spectroscopy.* Springer, 1999.

[37] S Reineke. White organic light-emitting diodes with fluorescent tube efficiency. *Nature*, 459:234–238, 2009.

[38] C Adachi, MA Baldo, ME Thompson, and SR Forrest. Nearly 100% internal phosphorescence efficiency in an organic light-emitting device. *J Appl Phys*, 90:5048–5051, 2001.

[39] M Meier. Emission characteristics of two-dimensional organic photonic crystal lasers fabricated by replica molding. *J Appl Phys*, 86:3502–3507, 2001.

[40] M Notomi, H Suzuki, and T Tamamura. Directional lasing oscillation of two-dimensional organic photonic crystal lasers at several photonic band gaps. *Appl Phys Lett*, 78:1325–1322, 2001.

[41] JR Tishler, MS Bradley, V Bulović abd JH Song, and A Nurmikko. Strong coupling in a microcavity led. *Phys. Rev. Lett.*, 95:36491, 2005.

[42] S Kéna-Cohen and SR Forrest. Room-temperature polariton lasing in an organic single-crystal microcavity. *Nat Photonics*, 4:371–375, 2010.

[43] Jelena Vučković, Marko Lončar, Hideo Mabuchi, and Axel Scherer. Design of photonic crystal microcavities for cavity qed. *Phys. Rev. E*, 65(1):016608, Dec 2001.

[44] EL Ru and PG Etchegion. *Principles of Surface-Enhanced Raman Spectroscopy: and related plasmonic effects.* Elsevier Science, 2008.

[45] M Lončar, A Scherer, and Y Qiu. Photonic crystal laser source for chemical detection. *Appl Phys Lett*, 82:4648–4650, 2003.

[46] E Yablonovitch. Inhibited spontaneous emission in solid-state physics and electronics. *Phys. Rev. Lett.*, 58:2059–2062, 1987.

[47] J Martorell and NM Lawandy. Observation of inhibited spontaneous emission in a periodic dielectric structure. *Phys. Rev. Lett.*, 65:1877–1880, 1990.

[48] EP Petrov, VN Bogomolov, II Kalosha, and SV Gaponenko. Spontaneous emission of organic molecules embedded in a photonic crystal. *Phys. Rev. Lett.*, 71:77–80, 1998.

[49] P. Lodahl. Controlling the dynamics of spontaneous emission from quantum dots by photonic crystals. *Nature*, 430:654–657, 2004.

[50] RC Mcphedran. Density of state functions for photonic crystals. *Phys. Rev. E*, 69:016609, 2004.

[51] Jeongwon Lee, Bo Zhen, Song-Liang Chua, Wenjun Qiu, John D. Joannopoulos, Marin Soljačić, and Ofer Shapira. Observation and differentiation of unique high-Q optical resonances near zero wave vector in macroscopic photonic crystal slabs. *Phys. Rev. Lett.*, 109:067401, Aug 2012.

[52] Z Li and D Psaltis. Optofluidic dye lasers. *Microfluid nanofluidics*, 4:145–158, 2008.

[53] SI Shopova, H Zhou, X fan, and P Zhang. Optofluidic ring resonator based dye laser. *Appl. Phys. Lett.*, 90:221101, 2007.

[54] M Gersborg-Hansen and A Kristensen. Tunability of optofluidic distributed feedback dye lasers. *Opt. Express*, 15:137–142, 2007.

[55] FP Shäfer. *Dye lasers.* Springer, 1990.

[56] Nikhil Ganesh, Wei Zhang, Patrick C. Mathias, Edmond Chow, SoaresJ. A. N. T., Viktor Malyarchuk, Adam D. Smith, and Brian T. Cunningham. Enhanced fluorescence emission from quantum dots on a photonic crystal surface. *Nature Nanotech.*, 2(8):515–520, 08 2007.

[57] Nikhil Ganesh, Wei Zhang, Patrick C. Mathias, Edmond Chow, SoaresJ. A. N. T., Viktor Malyarchuk, Adam D. Smith, and Brian T. Cunningham. Leaky-mode assisted fluorescence extraction: application to fluorescence enhancement biosensors. *Opt. Express*, 16:21626–21640, 2008.

[58] A Pokhriyal. Photonic crystal enhanced fluorescence using a quartz substrate to reduce limits of detection. *Opt. Express*, 18:24793–24808, 2010.

[59] A Penzkofer and W Leupacher. Fluorescence behavior of highly concentrated rhodamine r6g solutions. *J. Lumin*, 37:61–72, 1987.

[60] Shanhui Fan, Wonjoo Suh, and J. D. Joannopoulos. Temporal coupled-mode theory for the fano resonance in optical resonators. *J. Opt. Soc. Am. A*, 20(3):569–572, Mar 2003.

[61] L Novotny and B Hecht. *Principles of Nano-Optics.* Cambridge University Press, 2006.

[62] A Messiah. *Quantum Mechanics.* Wiley, 1976.

[63] S. Fan, PR Villeneuve, JD Joannopoulos, and EF Schubert. High extraction efficiency of spontaneous emission from slabs of photonic crystals. *Phys. Rev. Lett.*, 78:3294–3297, 1997.

[64] Jelena Vučković, Oskar Painter, Yong Xu, A Yariv, and Axel Scherer. Finite-difference time-domain calculation of the spontaneous emission coupling factor in optical microcavities. *IEEE J Quantum Electron*, 35:1168–1175, 1999.

[65] Yong Xu, RK Lee, and A Yariv. Finite-difference time-domain analysis of spontaneous emission in a microdisk cavity. *Phys. Rev. A*, 61:033808, 2000.

[66] C Shen, K Michielsen, and H De Raedt. Spontaneous-emission rate in microcavities: application to two-dimensional photonic crystals. *Phys. Rev. Lett.*, 96:120401, 2006.

[67] Y Zhang. High-q/v air-mode photonic crystal cavities at microwave frequencies. *Opt Express*, 19:9371–9377, 2011.

[68] F Wijnands. Green's functions for maxwell's equations: application to spontaneous emission. *Opt Quant Electron*, 29:199–216, 1997.

[69] Yong Xu, RK Lee, and A Yariv. Quantum analysis and the classical analysis of spontaneous emission in a microcavity. *Phys. Rev. A*, 61:033807, 2000.

[70] Kazuaki Sakoda. *Optical properties of photonic crystals*, volume 80. Springer, 2005.

[71] A Lagendijk and BA van Tiggelen. Resonant multiple scattering of light. *Phys. Rep.*, 270:143–215, 1996.

[72] PW Milonni. Semiclassical and quantum-electrodynamical approaches in nonrelativistic radiation theory. *Phys. Rep.*, 25:1–81, 1976.

[73] TJ Seok. Radiation engineering of optical antennas for maximum field enhancement. *Nano Letters*, 11:2606–2610, 2011.

[74] Song-Liang Chua, Ling Lu, Jorge Bravo-Abad, John D Joannopoulos, and Marin Soljačić. Larger-area single-mode photonic crystal surface-emitting lasers enabled by an accidental dirac point. *Optics letters*, 39(7):2072–2075, 2014.

[75] Y Liang. Three-dimensional coupled-wave analysis for square-lattice photonic crystal surface emitting lasers with transverse-electric polarization: finite-size effects. *Opt. Express*, 20:15945–15961, 2012.

[76] Ad Lagendijk, Bart van Tiggelen, and Diederik S. Wiersma. Fifty years of anderson localization. *Phys. Today*, 62(8):24–29, 2009.

[77] Yonatan Plotnik, Or Peleg, Felix Dreisow, Matthias Heinrich, Stefan Nolte, Alexander Szameit, and Mordechai Segev. Experimental observation of optical bound states in the continuum. *Phys. Rev. Lett.*, 107:183901, Oct 2011.

[78] Chia Wei Hsu, Bo Zhen, Song-Liang Chua, Steven G Johnson, John D. Joannopoulos, and Marin Soljačić. Bloch surface eigenstates within the radiation continuum. *Light: Science & Applications*, 2:e84, 2013.

[79] Peter D. Hislop and Israel Michael Sigal. *Introduction to Spectral Theory: with Applications to Schrödinger Operators*. Springer Verlag, 1996.

[80] J. von Neumann and E. Wigner. Über merkwürdige diskrete eigenwerte. *Phys. Z.*, 30(15):465–467, 1929.

[81] Allen Taflove and Susan C. Hagness. *Computational electrodynamics: the finite-difference time-domain method*. Artech House, 3 edition, 2005.

[82] Steven G. Johnson and J. D. Joannopoulos. Block-iterative frequency-domain methods for maxwell's equations in a planewave basis. *Opt. Express*, 8(3):173–190, 2001.

[83] Evgeny N. Bulgakov and Almas F. Sadreev. Bound states in the continuum in photonic waveguides inspired by defects. *Phys. Rev. B*, 78:075105, Aug 2008.

[84] G. Corrielli, G. Della Valle, A. Crespi, R. Osellame, and S. Longhi. Observation of surface states with algebraic localization. *Phys. Rev. Lett.*, 111:220403, Nov 2013.

[85] Steffen Weimann, Yi Xu, Robert Keil, Andrey E. Miroshnichenko, Andreas Tünnermann, Stefan Nolte, Andrey A. Sukhorukov, Alexander Szameit, and Yuri S. Kivshar. Compact surface Fano states embedded in the continuum of waveguide arrays. *Phys. Rev. Lett.*, 111:240403, Dec 2013.

[86] D. V. Evans, M. Levitin, and D. Vassiliev. Existence theorems for trapped modes. *J. Fluid Mech.*, 261:21–31, 1994.

[87] Victor Liu, Michelle Povinelli, and Shanhui Fan. Resonance-enhanced optical forces between coupled photonic crystal slabs. *Opt. Express*, 17(24):21897–21909, Nov 2009.

[88] Yi Yang, Chao Peng, Yong Liang, Zhengbin Li, and Susumu Noda. Analytical perspective for bound states in the continuum in photonic crystal slabs. *Phys. Rev. Lett.*, 113:037401, Jul 2014.

[89] Qiwen Zhan. Cylindrical vector beams: from mathematical concepts to applications. *Adv. Opt. Photon.*, 1(1):1–57, Jan 2009.

[90] N David Mermin. The topological theory of defects in ordered media. *Reviews of Modern Physics*, 51(3):591, 1979.

[91] Russell J Donnelly. *Quantized vortices in helium II*, volume 2. Cambridge University Press, 1991.

[92] M.V. Berry. The adiabatic phase and pancharatnam's phase for polarized light. *Journal of Modern Optics*, 34(11):1401–1407, 1987.

[93] Juan L Mañes, Francisco Guinea, and María AH Vozmediano. Existence and topological stability of fermi points in multilayered graphene. *Physical Review B*, 75(15):155424, 2007.

[94] Seita Iwahashi, Yoshitaka Kurosaka, Kyosuke Sakai, Kyoko Kitamura, Naoki Takayama, and Susumu Noda. Higher-order vector beams produced by photonic-crystal lasers. *Opt. Express*, 19(13):11963–11968, Jun 2011.

[95] Yoshitaka Kurosaka, Seita Iwahashi, Yong Liang, Kyosuke Sakai, Eiji Miyai, Wataru Kunishi, Dai Ohnishi, and Susumu Noda. On-chip beam-steering photonic-crystal lasers. *Nature Photonics*, 4(7):447–450, 2010.

[96] Kyoko Kitamura, Kyosuke Sakai, Naoki Takayama, Masaya Nishimoto, and Susumu Noda. Focusing properties of vector vortex beams emitted by photonic-crystal lasers. *Opt. Lett.*, 37(12):2421–2423, Jun 2012.